

ACCELERATOR MASS SPECTROMETRY AND RADIOISOTOPE DETECTION
AT THE
ARGONNE FN TANDEM FACILITY

MASTER

by

Walter Henning, Walter Kutschera, Michael Paul,
Robert K. Smither, Edward J. Stephenson and Jan L. Yntema

Prepared for
Fifth Tandem Conference
Catania, Italy
June 9-12, 1980



ARGONNE NATIONAL LABORATORY, ARGONNE, ILLINOIS

**Operated under Contract W-31-109-Eng-38 for the
U. S. DEPARTMENT OF ENERGY**

DISTRIBUTION OF THIS DOCUMENT IS UNLIMITED

ACCELERATOR MASS SPECTROMETRY AND RADIOISOTOPE DETECTION AT THE
ARGONNE FN TANDEM FACILITY

WALTER HENNING, WALTER KUTSCHERA, MICHAEL PAUL,[†] ROBERT K. SMITHER,
EDWARD J. STEPHENSON^{††} and JAN L. YNTEMA

Argonne National Laboratory, Argonne, Illinois 60439, USA[‡]

The Argonne FN tandem accelerator and standard components of its experimental heavy-ion research facility, have been used as a highly-sensitive mass spectrometer to detect several long-lived radioisotopes and measure their concentration by counting of accelerated ions.

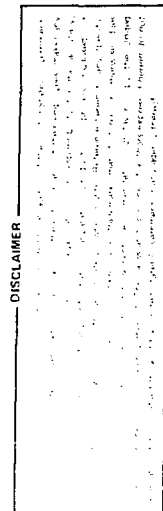
Background beams from isobaric nuclei have been eliminated by combining the dispersion from the energy loss in a uniform Al foil stack with the momentum resolution of an Enge split-pole magnetic spectrograph.

Radioisotope concentrations in the following ranges have been measured: $^{14}\text{C}/^{12}\text{C} = 10^{-12}$ to 10^{-13} , $^{26}\text{Al}/^{27}\text{Al} = 10^{-10}$ to 10^{-12} , $^{32}\text{Si}/\text{Si} = 10^{-8}$ to 10^{-14} , $^{36}\text{Cl}/\text{Cl} = 10^{-10}$ to 10^{-11} . Particular emphasis was put on exploring to what extent the technique of identifying and counting individual ions in an accelerator beam can be conveniently used to determine nuclear quantities of interest when their measurement involves very low radioisotope concentrations. We are able to demonstrate the usefulness of this method by measuring the $^{26}\text{Mg}(p,n)^{26}\text{Al}(7.2 \times 10^5 \text{ yr})$ cross section at proton energies in the astrophysically interesting range just above threshold, and by determining the previously poorly known half life of ^{32}Si .

[†]Present address: Racah Institute of Physics, Hebrew University of Jerusalem, Jerusalem, Israel

^{††}Present address: Indiana University Cyclotron Facility, Bloomington, Indiana 47405, U.S.A.

[‡]Work performed under the auspices of the Division of Basic Energy Sciences of the U.S. Department of Energy.



286

1. Introduction

The usefulness of particle accelerators as mass spectrometers has long been recognized and actually demonstrated at the very early stage of accelerator development¹⁾. However, applications of this technique were limited due to the fact that most accelerators were built for light-ion beam production. And even for those machines that were capable of accelerating heavier ions, the lack of heavy-ion detection and identification techniques would have severely limited their actual use for mass separation applications.

With the advent of heavy-ion accelerator and ion source technology as well as heavy ion detection techniques due to the recent interest in heavy ion nuclear physics, this situation has changed considerably. In 1977 it was demonstrated at three laboratories²⁻⁴⁾ and subsequently at various other research institutions⁵⁻⁷⁾, that present heavy-ion research facilities can be effectively used as ultra-sensitive mass spectrometers, and in particular are capable of quantitatively measuring very small radioisotope concentrations, in some cases as low as 10^{-16} .

Three characteristic features of these heavy-ion facilities are responsible for the drastic improvement in sensitivity and mass separation over conventional mass spectrometers: i) the higher energy available, typically several tens to hundreds of MeV per ion, allows the determination of the nuclear charge Z by the well established technique of differential energy loss measurements. The Z separation obtainable depends on incident energy and the mass region that one is working in. If one makes use of multiple differential energy loss measurements, it is possible for heavy-ions with $Z \leq 16$ and few MeV/nucleon incident energy to identify as few as 1 in 10^8 ions between neighboring Z 's. The nuclear charge resolution in effect can result in

mass separation at the same level since it separates isobars which are close in mass but possess different nuclear charge. ii) The higher energies allow the use of thin foils to break up background molecules, without deterioration of the beam quality that would affect the mass resolution. Background molecules of masses close to that of the ion of interest constitute a severe limitation in conventional mass spectrometry, in particular for heavy nuclei. The insertion of stripper foils essentially eliminates the molecular ions; the fragments will in general have drastically different ion-optical characteristics and can be separated. iii) The selectivity in the formation of charged particles in the ion source (in particular that of negative ions) and the ion-optical properties of the full accelerator system add another large factor in separation.

The limitations in accelerator mass spectrometry lie to some extent in the accuracy for detection efficiency. This is partly due to the complexity of the system, partly due to the fact that these facilities are used mainly for nuclear physics experiments and constantly undergo minor changes. One obvious solution is the construction of a dedicated facility as has been proposed and actually commenced for detection of radioisotopes (mainly ^{14}C) for dating purposes⁸⁾. On the other hand, the large number of operating heavy-ion facilities could provide a wider opportunity to apply this technique. At Argonne we have started a program of accelerator spectrometry which is aimed at exploring its usefulness under the constraints just indicated. In particular we have concentrated on two questions. First, to what extent can a heavy-ion facility with state-of-the-art but standard detection systems and minimal additional investment serve as a high-sensitivity mass-spectrometer? Second, to what extent can this capability be applied to measure radioisotope concentration for problems in nuclear physics

which are difficult to investigate with the more conventional methods?

2. Instrumental

2.1. GENERAL OUTLINE OF THE SYSTEM

The measurements described here were performed at the Argonne FN tandem accelerator facility⁹⁾. The FN tandem has been used over the last one and a half decades for nuclear physics experiments and undergone several steps in upgrading to provide high-quality heavy-ion beams. In particular the more recent technical improvements were aimed at providing stable heavy-ion beams of high quality and good transmission for injection into a superconducting linear post accelerator, presently under development¹⁰⁾. The measurements reported here were nearly exclusively performed with the FN tandem accelerator. Some very preliminary considerations on the possible use of the linac for mass spectrometry and some initial tests will be mentioned at the end of this article.

A schematic outline of the FN tandem and the experimental facility used in our mass spectrometry measurements is shown in fig. 1. Details of the individual components will be discussed in the subsequent sections. Schematically one can divide the system into 5 principal sections:

- 1) a negative-ion, inverted Cs-beam sputter source; ii) a beam transport from the ion source to the FN tandem, with a 40° inflection magnet that provides better than unit mass resolution up to masses $A \approx 80$ and selects the ion-mass of interest for injection into the accelerator; iii) the

upgraded FN tandem accelerator with a maximum of ≈ 9 MV acceleration voltage, and a foil-stripper in its terminal; iv) the beam transport between the FN tandem and the experimental facility, with a high-resolution 90° analyzing magnet, and v) the experimental setup to detect and identify individual ions, consisting of an Enge split-pole magnet spectrograph with an ionization-chamber type, position sensitive focal-plane gas detector.

The principal procedure to measure low radioisotope concentrations consists of accelerating, detecting and identifying individual radioisotope ions. The absolute concentration with respect, for example, to the stable isotopes is established by measuring the stable-isotope beam current from the same source sample. A second possibility to determine the radioisotope concentration of an unknown sample is to compare the measured ion-rate with that from a sample of known radioisotope concentration. The various operations involved in this procedure, and the details of the technical apparatus are discussed in the next sections.

2.2. DETAILS OF THE SYSTEM

2.2.1. Ion source.

The ion source used in the present measurements is a negative-ion Cs beam sputter source¹¹⁾. The specific geometry used here (fig. 2) of the sputter sample, incident sputter beam and extracted negative ion current

is known as inverted sputter source geometry and was developed by Chapman¹²⁾. Cesium is evaporated in a heatable reservoir and diffuses through the ring-shaped, porous tip of a heated tungsten ionizer. The positive Cs ions emerging from the tungsten tip are accelerated towards the sputter sample by 12 kV extraction voltage between the ionizer and the sputter sample. The positive Cs ions have a dual function: They act as the sputter beam to knock ions out of the sample material, and they provide a Cs coating on the sample surface which reduces the work function of the surface and increases the negative ion yield from the sample. The negative ions are extracted by the 12 kV extraction voltage through the center hole of the ring-shaped ionizer.

The various sputter samples (fig. 3) are held in a wheel which can be rotated around a horizontal axis to position different samples into the Cs beam. This sample wheel has 10 positions to hold disc-shaped sputter samples, which may for example be machined from solid material or consist of pellets pressed from powders. For our application, the simple geometry of a flat sample disc appears advantageous over that of the conical shape in the more conventional non-inverted sputter sources, in particular when very small samples are investigated. A similarly simple sputter sample arrangement is possible in the reflected Cs-beam geometry¹³⁾. We have found it very easy to prepare sputter pellets that were pressed from milligram amounts of material thoroughly mixed with binder materials like high-purity aluminum and zinc powder. In none of these cases were we pushing the lower limit of sample material necessary. Some detailed examples will be given in the later sections where specific radioisotopes are discussed.

2.2.2. Low-energy beam transport.

The low-energy injection system into the tandem (see fig. 1) serves two major functions: to match the beam acceptance phase ellipse of the accelerator and to provide some mass selection. The mass selection is provided by the 40° injection magnet approximately halfway between the ion-source and the first acceleration electrode. The magnet is double focussing and provides a mass resolution of approximately 1 in 80. This is sufficient for the mass range presently of interest, i.e. $A \lesssim 60$, to reduce neighboring background beams, which otherwise lead to unnecessary loading of the accelerator.

Except for the 40° injection magnet, all ion-optical components at the low-energy end of the tandem are electrostatic. As a consequence, for the fixed injection voltage of at present 132 kV achieved through pre-acceleration with two of the three NEC general-purpose accelerator tubes right after the ion source, all singly-charged negative ions will follow identical beam optics because they have identical energy versus charge ratio, E/q . This is important for the radioisotope measurements, where ratios are determined for beam currents, respectively ion rates from different isotopes. Mass-dependence in beam transmission due to the 40° injection magnet is minimized by the fact that the beam injected into the tandem has an emittance of $4 \text{ mm-mrad-MeV}^{\frac{1}{2}}$, which is at least a factor of two smaller than the acceptance of the accelerator.

The low-energy beam optics is as follows: The beam from the source will normally produce a waist following pre-acceleration. The waist location is chosen halfway to the 40° magnet. A 30-KV $2\frac{1}{2}$ " einzel lens close to the entrance of the 40° magnet provides a virtual object for the lens formed by the magnet and the electrostatic quadrupole triplet. The use of the electrostatic quadrupole triplet allows the production of the vertical

and horizontal waist at the same distance from the accelerator tube both with approximately a 1 mm radius. The divergence at this point is 10 mrad, and as a consequence the beam-spot size is approximately 2 mm in diameter. This beam is expected to produce a waist of 2 mm radius at the stripper in the tandem terminal; at 9 MV terminal voltage the divergence of the beam in the terminal prior to stripping is about 0.7 mrad. The multiple scattering in the foil will significantly increase the rms divergence of the beam, which will then determine the transmission through the FN accelerator.

2.2.3. FN tandem accelerator.

The Argonne FN tandem was installed in 1967 as a conversion from the smaller EN machine. It was installed with a 100% SF₆ insulating gas system, the first large tandem to do this. The accelerator was converted from a belt to a pelletron charging system in 1973, and at the same time the voltage dividing resistors were replaced by a separately pressurized corona tube. This resulted in a reliable operation with an excellent voltage stability. This feature is of great importance for the radioisotope measurements performed here, since under those conditions where only individual ions are accelerated, the lack of a measurable beam current will not allow the usual mode of stabilization with slit control currents. The accelerator has to be stabilized under such a "zero-beam" condition by a generating voltmeter and any inherent voltage stability of the accelerator will greatly improve the overall performance.

In late 1977, in preparation for the superconducting linac, the Argonne tandem underwent a major upgrading. The purpose of this upgrading was to improve the heavy-ion acceleration capability of the tandem. The inclined-field HVIC tube was replaced by one with straight, cylindrically symmetric optics manufactured by NEC, with permanent magnets placed in the

dead sections halfway between terminal and ground to suppress high-energy electrons. Together with the drastically-improved vacuum due to the all-ceramic and metal, bakable tubes, this led to a substantial improvement in heavy-ion transmission through the accelerator. For lighter heavy ions ($A \approx 10-40$) the transmission was measured to be as high as 70%, and for Ni ions it was found to be still 50%. For the mass-spectrometric purposes such high transmission is very desirable with respect to sensitivity but in particular also with respect to mass fractionation effects which will be less important if the overall transmission approaches unity. Mass fractionation is also minimized due to the straight geometry of the electrostatically-focussing accelerator tubes, particularly if one chooses ions for comparison, with identical or similar energy versus charge ratio, E/q .

There are two additional mass-fractionation effects of potential importance in the FN accelerator. The first has to do with the mass dependence of the beam emittance after terminal foil stripping due to the inverse mass dependence of the half-angle for small angle scattering. For neighboring isotopes around $A \approx 30$, this will lead to a few percent effect. Secondly, charge-change cross sections depend on ion velocity. Therefore neighboring isotopes may be chosen to have the same energy and electrostatic properties, but then the velocity will differ and consequently the charge-state distributions from the stripper foil. Yet another contribution to mass fractionation comes from the sputtering process in the ion source. The magnitude of the sum of all these effects was measured by comparing current ratios between stable isotopes of known abundances, as discussed later in some detail for specific examples (see sec. 3.3 and table IV).

2.2.4. High-energy beam transport.

The high-energy beam transport system delivers the fully accelerated heavy ion beam from the tandem exit to the target-chamber of the split-pole magnetic spectrograph. The major components (fig. 1) are 2 magnetic quadrupoles, three magnetic steerers, a 90° analyzing and a 30° switching magnet. Due to the exclusively magnetic beam focussing at the high-energy end, we chose in most cases to accelerate the radioisotope and the stable comparison isotopes to identical magnetic rigidity. Since the same ion charge state q was generally chosen, this implied reduced energies for the heavier isotopes to achieve constant magnetic rigidity $B\rho = (2mE/q^2)^{1/2}$. This introduced the mass fractionation discussed above, which needed to be determined experimentally from stable isotope ratio measurements.

Although all magnetic elements eliminate to a certain degree background beams of non-identical rigidity, the major separation comes from the high resolution 90° analyzing magnet, with $\Delta B\rho/B\rho = 10^{-3}$. In situations when the accelerator was stabilized by slit beam current control, i.e., for the stable isotope current measurements or for cases where the background beam from the unwanted stable isobar was very high (for example ^{32}S beams when measuring ^{32}Si ion rates) the object and image slits of the 90° analyzing magnet could be kept to the nominal setting for high resolution, i.e. 1.3 and 1.9 mm full width, respectively. When the tandem ran with the generating voltmeter (GVM) control the slits were generally opened by an additional factor of 3 to 4 to insure that no beam was lost due to accelerator voltage instabilities (see sec. 3 and fig. 11).

2.2.5. Split-pole magnetic spectrograph.

The beam current measurements for the stable isotopes, and the detection, identification and counting of individual radioisotope ions

was performed in the split-pole magnetic spectrograph system.¹⁴ As shown in Figure 4, it consists of two magnetic dipoles, a focal-plane detector vacuum box and a target-chamber with stainless-steel sliding seal. A beam tube is welded to the sliding seal that connects to the magnetic spectrograph. This allows a large angular motion of the spectrograph around the target center. In the radioisotope measurements usually an angle of 20° from the beam axis was chosen to set up the spectrograph and focal-plane detector system, and then the spectrograph was moved to 0° for radioisotope counting.

The stable isotope beam currents were measured by focussing the beam into an isolated Faraday cup with a biased electron suppression ring at -300 V in front of it. The beam was focussed to minimum beam spot size by requiring essentially zero beam current on a 3-mm diameter, isolated aperture directly in front of the Faraday cup and suppressor ring. No further collimation, except for wide-open apertures that act as scrapers for secondary beam particles scattered from the beam line walls, were allowed in the straight beam line section between the 30° switching magnet and the split-pole scattering chamber (see Fig. 1). For the detection of the radioisotope in the spectrograph at 0° , the complete Faraday cup assembly including suppressor ring and 3 mm aperture were retracted from the beam-line axis. The only collimation was from the entrance aperture of the split pole magnetic spectrograph. The beam diameter at that location is determined by the beam emittance, and in particular by the small-angle scattering from foils inserted in the target chamber for energy loss dispersion of background ions (see sec. 2.2.7.). For the Al foil stack used in most of our measurements, for ^{32}Si and ^{36}Cl at about 2 MeV/nucleon incident energy, we calculate a full angular width at half maximum due to small angle scattering of approximately 0.9° . This is considerably less than the maximum opening

angle of 2.9° (horizontal) \times 2.3° (vertical), as determined by the split pole entrance aperture. It was also verified experimentally that losses caused by this aperture are indeed negligible, by measuring ion rates in the split-pole with different apertures and observing a saturation for the largest opening. The effects from the beam emittance are negligible since the beam divergence at 3 mm full spot size was measured to be less than ± 2 mrad for ions in the mass range investigated so far.

2.2.6. Spectrograph focal-plane detector.

Basically, the detector¹⁵⁾ is a combination of a gridded ionization chamber and a proportional counter, but it also incorporates some features of drift chambers. A cross section of the counter is shown in fig. 5. Incident ions arrive at the detector from the left and are stopped in the gas volume within the central part of the counter. About 10^6 electrons and positive ions are generated along the particle path. An electric field causes the electrons to drift upward toward the grid structure and the anode planes, where various signals are generated. The position of the incident ion along the focal plane is measured by a resistive-wire proportional counter which is embedded in the anode plane. The position information is extracted by means of the rise-time difference technique of Borkowski and Kopp¹⁶⁾. The anode wire is a carbon-coated silica filament. The wire labeled "position 1" in fig. 5 is arranged to lie along the focal surface of the magnetic spectrograph. The anode wire is 72 cm long, which gives about 50 cm of useful distance along the focal surface. A second resistive-wire proportional counter at a distance of 4.4 cm from the first is used to determine the angle of incidence at the detector, but was not used in the present measurements.

The ΔE signal is derived by measuring the electric charge which is collected on the electrodes labelled ΔE_1 and ΔE_2 in the anode plane; the operation of this part of the detector is thus that of a conventional ionization chamber.

The total-energy signal E_{total} is measured by the use of the double-grid technique¹⁷⁾. This technique depends on an extra grid which is ac coupled to the cathode so that the region in which incident ions are stopped forms essentially a Faraday cage. No signal will appear in the output of the total-energy preamplifier until electrons from the primary ionization event drift beyond grid 1. After all electrons have drifted past grid 2, the charge collected by the preamplifier is proportional to the total energy of the incident ion.

The entire counter is surrounded by a vacuum-tight box to contain pure isobutane counter gas. The pressure of the flowing gas is kept constant by a Cartesian manostat and adjusted to stop the ions of interest in the active counter volume. The entrance window consists of clear mylar foil. The counter is mounted on a movable structure inside the vacuum chamber which positions it into the focal surface of the magnetic spectrograph. The principal operation of the focal plane detector is illustrated with an example in fig. 6. Here various reaction products were detected from the reaction $^{18}\text{O} + ^{40}\text{Ca}$ at 56 MeV incident energy. The differential energy loss ΔE which depends on the nuclear charge of the incident ion serves to identify its atomic number Z . For a selected Z , the total energy E as a function of focal plane distance $B\rho$ depends on the mass and the effective charge state q of the detected ion according to the relation $B\rho = (2mE/q^2)^{1/2}$. For the lighter heavy ions investigated here ($A \approx 10-40$), the quadratic dependence of the integer-valued q in general removes most ambiguities about the effective charge state. As a consequence the accurate measurement of

Bo to approximately 0.1–0.2%, and of E to approximately 1% allows the unambiguous determination of the particle mass m as illustrated in fig. 6.

2.2.7. Charge and energy loss dispersion in foils.

A major limitation of the detector besides those set by the resolution, is the maximum count rate that it can handle, typically 3 kHz. In particular when the spectrograph is operated at 0° , large background count rates can arise. This is due to the fact that in general background beams exist with the same magnetic rigidity as that of the radioisotopes detected, and consequently they will not be eliminated by the magnetic elements in the high-energy beam transport. These background beams arise from various charge-changing processes in the accelerator tube which will lead to an essentially "white" spectrum of in particular light heavy ions like ^{16}O and ^{12}C , which are always present, for example, from molecules injected into the tandem.

Two simple methods have proven effective to reduce the number of background ions incident on the focal plane detector, both of which involve the insertion of a foil in the target position of the split-pole scattering chamber. The first makes use of the charge-state dispersion introduced by a thin foil, typically $50\text{ }\mu\text{g}/\text{cm}^2$ Au on $10\text{ }\mu\text{g}/\text{cm}^2$ C. The change in charge-state experienced by the radioisotope and the background ion in passing through the thin foil, will generally remove the degeneracy in magnetic rigidity. The magnetic field in the split-pole spectrograph will then deflect the background ions away from the detector where they can be physically shielded. In order to maintain the resolution, the foil is kept rather thin to minimize the differential energy loss. Just the

opposite is sought when we use the energy loss dispersion by a foil as a function of Z to remove unwanted background beams. This is necessary in order to separate isobars, which in general will also exist with the same charge state as the radioisotope of interest (except for fully stripped ions if the radioisotope has the larger atomic number). Some examples are the ever-present ^{32}S and ^{36}S backgrounds in measurements of the ^{32}Si and ^{36}Cl radioisotopes as discussed later in detail. Insertion of a thick absorber foil will shift the energies of the two isobars by different amounts and consequently result in a different magnetic rigidity. Again, the background ions can be deflected off the detector face and physically shielded.

Figure 7 shows schematically the energy loss dispersion method for the separation of the ^{36}Cl radioisotope from ^{36}S background. The two ions are ion-optically indistinguishable for all of the beam transport up to the split-pole target chamber. There an aluminum absorber, actually a stack of 15 aluminum foils each $100\text{ }\mu\text{g}/\text{cm}^2$ thick, introduces an energy loss that leads to a different magnetic deflection in the split-pole magnets. Figure 8 shows the resulting focal plane position spectrum for various absorber materials which immediately illustrates the experimental problems associated with this method. The energy loss in the foil leads of course to an energy loss straggling due to the statistical nature of the loss mechanism. In particular because the differential energy loss of ions depends on their effective charge, the energy loss distribution of heavy ions is influenced by fluctuations in this effective charge. For the type of ions and energy ranges discussed here, it has been demonstrated experimentally that "charge-changing straggling" is the dominant contribution to the measured straggling width¹⁸⁾.

To first approximation the full straggling width at half maximum $\delta E_{1/2}$ is proportional to the square root of the foil thickness t . For a constant differential energy loss dE/dx , the total energy loss ΔE in the foil is proportional to t , and as a consequence the ratio of straggling width $\delta E_{1/2}$ to the energy loss difference, $\delta(\Delta E)$, between two ions decreases with increasing absorber foil thickness. For a given incident energy, however, the foil thickness cannot be increased arbitrarily, because the differential energy loss is not constant with energy but rather decreases with decreasing energy and thus there exists an optimum absorber thickness for the ratio $\delta E_{1/2}/\delta(\Delta E)$ ¹⁹⁾. In principle one can calculate this ratio for different absorber materials and thicknesses and optimize the foil choice. We have performed such calculations, for example, for 70 MeV incident ^{32}Si and ^{32}S ions. Requiring that half the incident energy is lost in an absorber foil, the ratio $\delta E_{1/2}/\delta(\Delta E)$ decreases by nearly a factor of two between a Au foil and a carbon foil. The lower Z carbon foil seems an optimal choice.

However, the energy broadening is often dominated by effects other than the shape of the straggling distribution, namely foil inhomogeneities, pinholes, voids, etc. In addition, as seen in fig. 8, the relevant line width may not be so much that at half maximum but rather that in the tails of the line. We have therefore measured energy loss straggling in various absorber materials and thicknesses to find an optimum absorber foil. Figure 9 shows results for 72 MeV ^{28}Si ions incident on various foils. Particular effort was spent to reduce possible inhomogeneities by using stacks of many thin foils to average out local thickness variations, rather than one single thick foil.

In fig. 9a we have plotted the ratio between the experimentally observed energy width $\delta E_{1/2}$ and the mean total energy loss $\overline{\Delta E}$, versus $\overline{\Delta E}$. From an experimental point of view, we want to minimize this ratio. We find that the best ratio is obtained for an aluminum foil stack consisting of 15 foils, each $100 \mu\text{g}/\text{cm}^2$ thick. The good quality of the aluminum foil stack in an absolute sense becomes also evident in fig. 9b where the measured straggling widths are compared to theoretical values, calculated with the empirical expression given in ref. 20). The aluminum foil comes close to the calculated value indicating that additional broadening effects must be small. This is, however, also true for the gold foils. The situation is considerably worse for the other absorber foils. The fact that the gold foils, although close to the theoretical straggling limit, do not perform much better than the carbon foils for the experimentally relevant ratio $\delta E_{1/2}/\overline{\Delta E}$ is of course a consequence of the fact that this ratio is expected to decrease with decreasing nuclear charge, as discussed above. In fig. 8 are shown as an example, the focal plane position spectra of $^{36}\text{Cl}^{13+}$ and $^{36}\text{S}^{13+}$ ions after passage of an 88-MeV incident $^{36}\text{Cl} + ^{36}\text{S}$ beam through various absorber foils. The best separation between the isobaric ^{36}Cl and ^{36}S ions is achieved with the Al foil stack, which also produces minimum tailing.

In fig. 10 we have plotted results of straggling width measurements for 80-MeV ions between ^{27}Al and ^{37}Cl incident on the aluminum foil stack. To take out the dependences on target and projectile charges, the reduced straggling widths, $\delta E_{1/2}^0$, as defined in ref. 20 are plotted. As expected, the foil stack yields experimental straggling widths for all ions near the predicted values. It seems though that the dependence of $\delta E_{1/2}^0$ on $\overline{\Delta E}$ increases somewhat slower than that predicted by the empirical expressions in ref. 20). The aluminum foil stack was used in all the radioisotope measurements discussed in the subsequent sections whenever a thick absorber foil was necessary.

3. Performance and Results of Radioisotope Detection

As stated before, the radioisotope concentrations measured in our experiments were obtained by normalizing to the beam currents of stable isotopes from the same sample in the ion source. In order to make this measurement as close to the spectrograph as possible, the small Faraday cup discussed above, with suppressor ring and a 3-mm entrance aperture was interchanged in position with the energy-loss foil stack in front of the spectrograph, and alternately the stable isotope beam current in the Faraday cup and the radioisotope counting rate in the focal plane detector were measured. The complete focusing system from the ion source to the spectrograph was first set up with the stable-isotope beam by requiring the current on the entrance aperture of the Faraday cup to be close to zero. Then the 40° inflection magnet (see Fig. 1) was set to the radioisotope mass and the terminal voltage was changed in such a way as to match the magnetic rigidity of the stable-isotope beam. None of the other beam-optical elements were changed. The final settings of the inflection magnet and the terminal voltage were verified by scanning in small steps around the precalculated values and optimizing the counting rate of the radioisotope in the spectrograph. Figure 11 shows the result of this procedure for ^{14}C . The flat yield regions are both considerably wider than observed fluctuations. The entrance and exit slits of the 90° analyzing magnet were wide open and the terminal voltage stabilized with a generating voltmeter²¹⁾. An exception was the run with ^{32}Si where the ^{32}S background beam was strong enough to allow tandem stabilization by slit control. In the ^{32}Si measurements, the velocity of the ions at the terminal stripper was kept constant and the complete accelerator system was adjusted separately for $^{32}\text{Si} + ^{32}\text{S}$ and ^{28}Si by optimizing the beam current in the spectrograph Faraday cup.

Up to now, all changes have been made manually as in the routine operation of the tandem. It takes approximately 5 to 10 minutes to switch between radioisotope and stable isotope running condition. Although a computerized system might improve the precision in the switching procedure, other factors such as the current measurement of the stable-isotope beam and the background subtraction are the dominant contributions to the errors in the measured isotope concentrations. Various contributions to the errors are discussed in some detail in the specific examples presented in the subsequent section. From the overall reproducibility between various measurements we feel that absolute concentrations can be measured with an accuracy of 10–15%. We have not invested at this stage major efforts in attempting to obtain high accuracy for radioisotope measurements where calibrated standards are available (e.g. ^{14}C). Since we think that highest accuracy can probably be achieved reliably only at a dedicated facility, we have rather made use of the high sensitivity of the method to measure quantities that are of interest under the given limitation in accuracy.

At present we have detected and measured radioisotope concentrations between 10^{-8} and 10^{-14} for ^{14}C , ^{26}Al , ^{32}Si and ^{36}Cl . For ^{26}Al the method was used to measure the $^{26}\text{Mg}(p,n)^{26}\text{Al}$ cross section; for ^{32}Si we have applied this technique to directly determine its halflife. In the subsequent sections we discuss some details of the various measurements. The results of these measurements are presented in table I; typical running conditions of the accelerator system for the various isotopes are presented in table II.

3.1 MEASUREMENTS WITH ^{14}C

As discussed above, one of the major obstacles in accelerator spectroscopy is the sometimes overwhelming background beam from stable isobars. Fortunately, this problem does not exist for ^{14}C measurements with the tandem since ^{14}N does not form stable or sufficiently metastable negative ions²²⁾. Other residual background beams of identical magnetic rigidity could be greatly reduced by the charge-state dispersion with a thin stripper foil in the split-pole target chamber as discussed above. The focal plane detector was then clearly capable of separating and identifying the $^{14}\text{C}^{6+}$ ions as shown in fig. 12. The $^{13}\text{C}^{4+}$ stable isotope beam was used for normalization. Table I lists some of the samples investigated and the radio isotope concentrations measured. The recent charcoal sample originated from a piece of wood burned in a fireplace. Its ^{14}C concentration was independently measured from β activity; the agreement is satisfactory within error bars. We started some attempts to date charcoal samples from a Maya excavation site in Copán, Honduras, Central America. In this case, the accelerator value was determined relative to the recent charcoal sample using the precise decay counting value for calibration. The error in the accelerator value for the Maya sample is statistical, unfortunately quite large since only a short run was performed. Therefore, the excellent agreement with the decay counting result is not significant and must be confirmed by a more precise accelerator measurement. The $^{14}\text{C}/^{12}\text{C}$ ratio corresponds to a date of about 400 yr A.D. The so-called "Fermi" graphite sample in table I was obtained from stock graphite at Argonne and possibly used in the reactor CP1 by Enrico Fermi at the University of Chicago. Most of the ^{14}C was probably produced from $^{13}\text{C}(n,\gamma)^{14}\text{C}$.

Another graphite sample showed also a relatively high ^{14}C count rate. It seems unlikely that this is the inherent background from the ion source. At this stage we have not further pursued the question of the inherent ^{14}C background since most of our efforts were directed at the heavier radioisotopes.

3.2 MEASUREMENTS WITH ^{26}Al

Measurements of the ^{26}Al radioisotope were originally started because it seemed a convenient nucleus to explore the capabilities of accelerator mass spectrometry for heavier radioisotopes. Similar measurements have been recently performed with the linac-cyclotron accelerator system ALICE at Orsay²³⁾ and with the tandem accelerator at Rochester²⁴⁾.

$^{26}\text{Al}/^{27}\text{Al}$ ratios in the range from 10^{-10} to 10^{-12} have been measured.

One particular feature of ^{26}Al is that the stable isobar ^{26}Mg does not form negative ions which considerably reduces background problems. A convenient ^{26}Al source was available in the form of an aluminum beam stop from the 20-MeV electron linac at Argonne, where ^{26}Al has been formed over the years via the $^{27}\text{Al}(\gamma, n)^{26}\text{Al}$ reaction. From the known irradiation time, approximate total beam current and (γ, n) cross section curves we calculate an expected concentration of $^{26}\text{Al}/^{27}\text{Al} = 4 \times 10^{-10}$ which agrees well with an average concentration of $(4.2 \pm 0.2) \times 10^{-10}$ as measured by gamma-ray activity of the 1.8-MeV gamma-ray transition in the ^{26}Mg daughter nucleus. Our values of $(2.9 \pm 0.6) \times 10^{-10}$ and $(6.5 \pm 0.8) \times 10^{-10}$, as measured by direct mass spectrometry for two small milligram samples are in good agreement with these values. The variation in measured ^{26}Al concentration is attributed to the non-uniform distribution of the radioactivity in the beam stop (3 grams). Another test-sample was prepared by irradiating a ^{27}Al sample with 1×10^{17} ^{16}O ions of 56 MeV. The measured $^{26}\text{Al}/^{27}\text{Al}$ ratio corresponds to an integrated cross section for the

As an interesting application, the present system could be conveniently used for the $^{26}\text{Mg}(p,n)^{26}\text{Al}$ (7.2×10^5 yr) cross section measurement which is of astrophysical interest. The cross section values are of importance for the synthesis of ^{26}Al in thermonuclear reactions which has become of great interest due to the recent discovery of a significant isotopic excess of ^{26}Mg in Ca-Al rich inclusions from the Allende meteorite²⁵⁾. The observed correlation of ^{26}Mg excess with ^{27}Al abundance has been interpreted as the presence of ^{26}Al at the time of formation of these inclusions, and its subsequent decay in situ to produce ^{26}Mg . If this interpretation is correct, the $^{26}\text{Al}/^{27}\text{Al}$ ratio at the time of condensation was about 5×10^{-5} which must be compared to values of $\sim 10^{-3}$ (refs. 26,27) calculated for nucleosynthesis in a supernova. The short half-life of ^{26}Al then implies that such an event must have occurred no more than a few million years prior to the formation of these inclusions.

The $^{26}\text{Al}/^{27}\text{Al}$ ratio predicted by the nucleosynthesis calculation depends among other things critically on the cross section of the nuclear reactions involved, for example the $^{26}\text{Al}(n,p)^{26}\text{Mg}$ reaction which, however, requires a radioactive target. Instead the inverse reaction $^{26}\text{Mg}(p,n)^{26}\text{Al}$ has been studied to some extent in the thermonuclear relevant energy range 2 MeV above threshold. Measurements of the ground state production via radioactivity are difficult due to the long half-life of the ^{26}Al ground state. For example, the total number of ^{26}Al nuclei ($\sim 10^{10}$) involved in the measurements discussed here result in only one disintegration per hour. This seemed therefore a favorable case to apply the accelerator mass spectrometry technique developed here and to measure the cross section by determining the $^{26}\text{Al}/^{27}\text{Al}$ ratio. ^{26}Mg foils (99.4% isotopic abundance, 3.5–3.0 mg/cm² thick, ~ 1 mg total material) were bombarded with protons

from the Argonne FN tandem accelerator in the energy range from 5.3 to 7.0 MeV. Stacks of up to three foils were used. With an average beam current between 300 and 400 nA total proton charges between 1.4 and 3.7×10^{-3} Coulomb were collected in individual runs. The current measurement was independently checked by simultaneously bombarding a 4.5 mg/cm^2 thick Cu foil behind the stack and measuring the γ activity produced via $^{65}\text{Cu}(p,n)^{65}\text{Zn}$.

After the irradiation the foils were treated chemically and pellets were produced that contained the ^{26}Al ions uniformly distributed through the material. Since the sample preparation is an important step for a reliable measurement of a radioisotope concentration, in particular when small sample sizes -- one of the strengths of this method -- are involved, we will discuss it in some detail as a typical example. After the irradiation, ^{27}Al carrier powder (15-25 mg) was added to each of the ^{26}Mg foils and the mixture converted into oxide by dissolving the metals in HCl, adding NH_4OH to precipitate $\text{Mg}(\text{OH})_2$ and $\text{Al}(\text{OH})_3$, centrifuging and finally heating the hydroxides to about 400°C to obtain $\text{MgO} + \text{Al}_2\text{O}_3$. For a reliable analysis of the original ^{26}Al content, the only necessary requirement is that the ^{26}Al produced in the ^{26}Mg foils was converted to Al_2O_3 with the same efficiency as the added ^{27}Al . The $\text{MgO} + \text{Al}_2\text{O}_3$ powder (16 to 40 mg) was then thoroughly mixed with 140 mg Zn dust and pressed to solid pellets of 6.4 mm diameter. The various pellets were mounted on the 10-position cone wheel of the inverted Cs-beam sputter source.

The $^{26}\text{Al}/^{27}\text{Al}$ ratios were measured by first tuning the tandem to a 69.33-MeV $^{27}\text{Al}^{8+}$ beam. This beam was focussed into the interchangeable Faraday cup in the split-pole target chamber. Next the 40° inflection

magnet between ion source and tandem and the terminal voltage were changed to allow acceleration of 72-MeV $^{26}\text{Al}^{8+}$ ions which have the same magnetic rigidity as the previously tuned $^{27}\text{Al}^{8+}$ ions. The increased ion velocity was measured with ^{27}Al ions to result in a 4% increase of the 8^+ charge state probability in the terminal stripping process. The detection system was optimized with the ^{26}Al ions from the ion source sample machined from the aluminum beam stop. The $^{26}\text{Al}^{8+}$ ions from the tandem were stripped to $^{26}\text{Al}^{11+}$ by the $50\text{ }\mu\text{g}/\text{cm}^2$ Au foil in the split-pole scattering chamber and momentum analyzed at 0° . A value of 0.48 was measured for the 11^+ charge state probability with a ^{27}Al beam of equal velocity. The final settings for the 40° inflection magnet current and the terminal voltage were obtained by scanning in small steps around the precalculated values and optimizing the $^{26}\text{Al}^{11+}$ yield in the detector. Average conditions during the measurements of the various samples were (see table 11): 1.5 nA of $^{27}\text{Al}^-$ source current; 2.3 nA $^{27}\text{Al}^{8+}$ current after the tandem. The typical total counting rate in the focal plane detector was $\approx 30/\text{sec}$. The $^{27}\text{Al}^{8+}$ background current from a pellet made from pure Zn dust was less than 0.005 nA.

Figure 13 shows two-dimensional spectra of the total energy E_{total} versus differential energy loss ΔE for two samples (Table III). The $^{26}\text{Al}^{11+}$ peak is clearly separated from the background peaks of ^{27}Al and ^{26}Mg . ^{27}Al arises from the tail of $^{27}\text{Al}^-$ being accepted by the accelerator due to insufficient mass resolution of the 40° injector magnet and undergoing multiple charge-changing processes in the accelerator tube. This results in an energy gain for the ions leaving the tandem which matches the magnetic rigidity of the 72-MeV $^{26}\text{Al}^{8+}$ ions. Similarly, the ^{26}Mg peak originates from a tail of $^{26}\text{MgH}^-$ ions. It is unlikely that the ^{26}Mg peak is due to injected $^{26}\text{Mg}^-$ ions since there is evidence against the

existence of Mg^- ions²⁸⁾. The non-existence of Mg^- ions favors the use of a tandem for ^{26}Al measurements rather than accelerators which use positive ions, because of the otherwise overwhelming background from ^{26}Mg . (See however ref. 23 who use fully stripped Mg^{12+} and Al^{13+} ions for isobar separation). Table III gives the result of the $^{26}\text{Al}/^{27}\text{Al}$ ratio measurements and the cross section values. A discussion of the result is presented elsewhere²⁹⁾.

3.3 MEASUREMENTS WITH ^{32}Si

The ^{32}Si measurement was started from the very beginning⁹⁾ with the intention to measure the half-life which was only poorly known, by using the relation

$$T_{1/2} = \frac{N}{dN/dt} \ln 2$$

where N is the number of ^{32}Si nuclei in the sample and dN/dt the disintegration rate, which can be obtained from a measurement of the specific β activity.

The number N of ^{32}Si nuclei in the sample will be determined by the accelerator mass spectrometry method presented here. The half-life measurements have been completed in the meantime and the results have been submitted for publication³⁰⁾. Here we want only to discuss the aspects of the ^{32}Si concentration measurement.

The sample material was obtained from Brookhaven³¹⁾ where in 1968 approximately 15 mg of isotopically enriched SiO_2 (95.55% ^{30}Si) were bombarded with 3.4 MeV tritons from the 3.5 MV Van de Graaff accelerator for 300 hrs, for a total triton charge of 4.14 Coulomb. After three years of radiation cooling, the target material was converted into potassium fluosilicate, K_2SiF_6 . This was the material used in the present

study to prepare sputter targets. Sputter targets were prepared by mixing 1.5 to 3 mg of K_2SiF_6 with 100 mg Al or 200 mg Zn powder. This mixture was pressed into solid pellets of 6.4 mm diameter. Three different types of K_2SiF_6 were used, all chemically processed in the same way: one containing ^{32}Si , and two non-radioactive ones with natural isotopic Si abundance and enriched in ^{30}Si , respectively. The latter was important for determining the background beam from the Si impurity in the carrier materials by measuring ratios of ^{28}Si , ^{29}Si and ^{30}Si beam intensities and comparing them to the expected isotope ratios. Isotopic ratios were measured with the tandem acceleration voltage adjusted for equal ion velocity at the stripper position in order to reduce charge-state fractionation effects. We found that the Si background beam contributed less than 1% to the total Si current for the Zn carrier material, and between 15 and 35% for the various Al carrier materials. For the active K_2SiF_6 samples prepared with Al powder, the beam current measurements were corrected for the background beam. Table IV lists the results of the isotope ratio measurements.

$^{32}Si/Si$ ratios were measured by comparing the ^{32}Si ion rates, counted in the split-pole spectrograph at 0° , with the ^{28}Si current measured in a Faraday cup in front of the spectrograph. The major problem in counting ^{32}Si ions was a strong, ever-present isobaric background beam of ^{32}S . As discussed above, we used the Z dependence of the differential energy loss to disperse the energy of 80-MeV incident ^{32}Si and ^{32}S ions by the 1.5 mg/cm^2 thick uniform Al foil stack (15 foils) in front of the spectrograph. The energy loss difference of $\approx 4 \text{ MeV}$ resulted in a spatial separation of ^{32}Si and ^{32}S in the focal plane. The ^{32}S ions were then physically shielded from the focal plane detector by tantalum blocks.

This reduced the ^{32}S count rate from $10^7/\text{sec}$ to approximately $10^3/\text{sec}$. The residual ^{32}S background rate of $10^3/\text{sec}$ resulted from slit scattering, charge changing processes in the split-pole magnet chamber and other background effects; these residual ^{32}S ions were unambiguously separated from ^{32}Si ions by measuring the differential energy loss and the total energy of these ions in the focal plane detector (see figs. 14 and 15). Figure 16 shows focal plane position spectra for the various stages of analysis. In 16(a) the scattered ^{32}S ions are observed at $\theta_{\text{lab}} = 3^\circ$ for two charge states. When the spectrograph is moved to 0° , the intensity in these lines increases so enormously that they have to be physically shielded from the detector. The count rate at 0° in the region between the blocks and thus between the defined charge states arises from the tails of the lines and is still of the order of 1 kHz. The $\Delta E/E$ resolution illustrated in figs. 14 and 15, however, allows an unambiguous separation of the ^{32}Si peak from this background peak (fig. 16c). $^{32}\text{Si}^{9+}$ ions rather than the most abundant $11+$ ions were selected with the spectrograph in order to reduce the ^{32}S background rate. A $9+$ charge state probability of 6.7% for ^{32}Si was measured in the spectrograph with ^{30}Si ions of equal velocity emerging from the Al foil stack.

The $^{32}\text{Si}/\text{Si}$ ratios were measured by alternately tuning the accelerator system for a current measurement of 70 MeV $^{28}\text{Si}^{9+}$ ions (typically 1 nA) and for individual counting of 80 MeV $^{32}\text{Si}^{9+}$ ions. This ensured the same ion velocity at the terminal stripper ($5 \mu\text{g}/\text{cm}^2$ carbon foil) and therefore the same $9+$ charge-state probability. The uncertainty in the transmission efficiency through the tandem due to the use of two different terminal voltages was estimated to be less than 10% from our stable-isotope ratio measurements. Together with similar uncertainties in the absolute detection efficiency of the spectrograph and in the current measurements, all independent of each other, we find a total systematic error of $\pm 17\%$.

Figure 7 displays the results for the $^{32}\text{Si}/\text{Si}$ ratios obtained in three different runs. The total Si current was calculated from the measured ^{28}Si current and the isotope ratios discussed above. Individual measurements took from 10 to 55 minutes, with 170 to 3400 $^{32}\text{Si}^{9+}$ ions counted in the heavy ion detector. The plotted errors are statistical only. With an overall systematic uncertainty of $\pm 17\%$, the agreement between individual runs is satisfactory. Since the scatter of the individual measurements is primarily due to systematic uncertainties, the final $^{32}\text{Si}/\text{Si}$ ratio is calculated as the unweighted mean over all measurements, and the 17% systematic uncertainty is adopted as the final error. Thus, we obtain: $^{32}\text{Si}/\text{Si} = (2.82 \pm 0.50) \times 10^{-8}$.

The specific activity measurements and a discussion of the half life results are presented in ref.³⁰⁾. For completeness we list the half-life value found there:

$$T_{1/2}(^{32}\text{Si}) = 101 \pm 18 \text{ yr.}$$

This value is considerably shorter than the best previously measured values, obtained by geophysical methods, which yield half-life values of $T_{1/2} = 330 \pm 40 \text{ yr}$ (ref. 32) and $276 \pm 32 \text{ yr}$ (ref. 33).

The second ^{32}Si sample in table I was prepared by irradiating a Si single crystal with 4×10^{15} ^{18}O ions of 56 MeV. The ^{32}Si content corresponds to a cross section of the $^{30}\text{Si}(^{18}\text{O}, ^{16}\text{O})^{32}\text{Si}$ reaction of about 1 mb.

3.4 MEASUREMENTS WITH ^{36}Cl

^{36}Cl is the heaviest radioisotope investigated so far with the Argonne accelerator mass spectrometry system. The ^{36}S isobar is the dominant background beam; fortunately the natural ^{36}S abundance is only 10^{-4} of that of the ^{32}S abundance, so it is less of a problem to ^{36}Cl

to ^{32}Si . The other isobar, ^{36}Ar , does not form stable negative ions. Figures 18 and 19 show, similar to the ^{32}Si discussed above in detail, that by energy loss dispersion with the 1.5 mg Al foil stack and $\Delta E/E$ separation in the focal plane detector a complete separation of ^{36}Cl and ^{36}S is achieved (compare also fig. 8).

Several samples with known ^{36}Cl concentrations have been prepared by neutron irradiation of NaCl samples. They are listed in table 1. The results on the highly enriched samples agree well with the expected values in the last column, where the ^{36}Cl content was determined from the measured ^{24}Na activity and the known $^{23}\text{Na}(n,\gamma)$ and $^{35}\text{Cl}(n,\gamma)$ cross sections. The origin of the ^{36}Cl content in the blank sample is not known. The NaCl material was taken from a window for infrared spectroscopy. Typical running conditions were (see table II): $^{37}\text{Cl}^- = 30\text{-}40$ nA, $\text{TV} = 8$ MV, $^{37}\text{Cl}^{10+} = 1.4$ nA. For the highest enriched sample, the $^{36}\text{Cl}^{13+}$ counting rate in the focal plane detector was 10 counts/sec

4. Summary and Future Improvements

The Argonne tandem accelerator mass spectrometry system which is based on standard equipment of an experimental heavy-ion facility, has proven useful in determining radioisotope concentration from ^{14}C to ^{36}Cl in the range between 10^{-8} to 10^{-14} . No effort has been made to lower this limit in sensitivity at the present time, although we believe that an increase in sensitivity by 2 orders of magnitude could be achieved without too much additional investment. We have rather concentrated on applying the system in its present capability to study problems of interest to nuclear physics, which are difficult to investigate with the more conventional methods. The success in these measurements encourages us to apply this technique to other problems in nuclear physics and related fields.

In the near future we plan to expand the system by making use of the beam-bunching system at the Argonne tandem for an additional mass measurement by time-of-flight. We also plan to explore the capabilities that are offered by the higher energies from the superconducting post accelerator.¹⁰ Since the energy-loss difference, and as a consequence the range difference between Z's increases with energy (see fig. 20a), it is suggestive to use the linac for such measurements. The major difficulty that arises is the phase stability between injected beam-pulses and the linac acceleration field, which is normally assured by a phase-lock system which senses the actual beam arrival time³⁴). In some preliminary tests, we attempted to accelerate and identify ions of the radioisotope ^{32}Si studied previously at the tandem, with only a few picoamperes background beam from the isobaric ^{32}S . We found that the adjusted phase-lock system ran stably on charge currents of 10 pA $^{32}\text{S}^{14+}$.

The ^{32}Si ions were separated from ^{32}S through an energy range measurement at a beam energy of 230 MeV. In fig. 20b, we plot the normalized yield for events detected in a ΔE -E Si surface barrier detector telescope (5μ , 100μ) at 0° behind a gold-absorber of variable thickness. The yield is normalized to the ^{32}S background beam. An excess of ions is transmitted through the thickest Au-absorber when the beam originates from a sample in the tandem sputter source that contains ^{32}Si . The ΔE signals for these events are consistent with those expected for ^{32}Si .

The higher beam energies from the superconducting linac will also allow isobar separation by fully stripping the ions. In the near future, the following isobar pairs will be accessible to fully stripping with reasonable efficiency ($>1\%$): $^{26}\text{Al}(T_{1/2} = 7.2 \times 10^5 \text{ yr}) - ^{26}\text{Mg}$ (see ref. 23), $^{41}\text{Ca}(1.0 \times 10^5 \text{ yr}) - ^{41}\text{K}$, $^{53}\text{Mn}(3.7 \times 10^6 \text{ yr}) - ^{53}\text{Cr}$ and
(see ref. 38)

^{59}Ni (7.5×10^4 yr) - ^{59}Co . As mentioned above, the phase-lock system requires a "macroscopic" beam of the order of a few tens of pA to reliably synchronize the bunching system with the rf of the linac. Such a pilot beam can be conveniently supplied by the stable isobar. This would also guarantee a more reliable stabilization of the tandem by slit-control rather than by GVM control, which is required for the "zero-beam" mode. However, it has to be seen whether fully stripping with subsequent charge state separation can sufficiently separate the radioisotope from the strong pilot-beam background.

Acknowledgement

The success of experiments with accelerator mass spectrometry depends to a high degree on the support from the technical staff. We should like to thank P. J. Billquist for preparation of the ion source, P. Den Hartog and the tandem crew for a skillful operation of the accelerator and G. E. Thomas, Jr. for the preparation of absorber foils and sputter pellets. The continuing help of I. Ahmad in various chemical and radiochemical problems and encouraging discussions with R. Middleton, J. P. Schiffer and C. M. Stevens are gratefully acknowledged.

References

- 1) L. W. Alvarez and R. Cornog, Phys. Rev. 56 (1939) 379; and Phys. Rev. 56 (1939) 613.
- 2) R. A. Muller, Science 196 (1977) 489.
- 3) D. E. Nelson, R. G. Korteling and W. R. Stott, Science 198 (1977) 507.
- 4) C. L. Bennet, R. P. Beukens, M. R. Clover, H. E. Gove, R. P. Liebert, A. E. Litherland, K. H. Purser and W. E. Sondheim, Science 198 (1977) 508.
- 5) Proc. First Conference on Radiocarbon Dating with Accelerators, Rochester, 20-21 April 1978, ed. H. E. Gove.
- 6) Proc. 10th International Radiocarbon Conference, Bern/Heidelberg, 19-26 August 1979, Radiocarbon (1980), in press.
- 7) For recent review articles see R. A. Muller, Physics Today 32 (1979) 23; C. L. Bennet, American Scientist 67 (1979) 450; K. H. Purser, A. E. Litherland and H. E. Gove, Nucl. Instrum. Methods 162 (1979) 637; T. S. Mast and R. A. Muller, Nucl. Science Applications, to be published; A. E. Litherland, Am. Rev. of Nucl. Part. Sci., to be published.
- 8) K. H. Purser, R. B. Liebert and C. J. Russo, see ref. 6.
- 9) W. Kutschera, W. Henning, M. Paul, E. J. Stephenson and J. L. Yntema, see ref. 6.
- 10) K. W. Shepard, IEEE Trans. Nucl. Sci. NS-26 (1979) 3659; L. M. Bollinger, Proc. Symposium on Heavy Ion Physics from 10 to 200 MeV, Brookhaven.
- 11) R. Middleton and C. Adams, Nucl. Instrum. Methods 118 (1974) 329.
- 12) K. R. Chapman, IEEE Trans. Nucl. Sci. NS-23 (1976) 1109.
- 13) K. Brand, Nucl. Instrum. Methods 141 (1977) 519; and Rev. Phys. Appl. 12 (1977) 1453.

- 14) J.E. Spencer and H. A. Enge, Nucl. Instr. Methods 49 (1967) 181.
- 15) J. R. Erskine, T. H. Braid and J. C. Stoltzfus, Nucl. Instrum. Methods 135 (1976) 67.
- 16) C. J. Borkowski and M. K. Kopp, Rev. Sci. Instrum. 39 (1968) 1515.
- 17) D. Shapiro, R. M. DeVries, H. W. Fulbright, J. Toke and M. R. Clover, Nucl. Instrum. Methods 129 (1975) 123.
- 18) O. Vollmer, Nucl. Instrum. Methods 121 (1974) 373.
- 19) H. G. Clerc, H.-H. Schmidt, H. Wohlfarth, W. Lang, H. Schrader, K. E. Pferdekämpfer, R. Jungmann, M. Ashgar, J. P. Bocquet and G. Siegert, Nucl. Instrum. Methods 124 (1975) 607.
- 20) H. Schmidt-Böcking, in Lecture Notes in Physics, Vol. 83, p. 81 Springer-Verlag, Berlin (1978).
- 21) W. K. Brookshier, J. R. Wallace and A. Langsdorf, IEEE Trans. Nucl. Sci. NS-18 (1971) 101.
- 22) K. H. Purser, R. B. Liebert, A. E. Litherland, R. P. Beukens, H. E. Gove, C. L. Bennett, M. R. Clover, and W. E. Sondheim, Rev. Phys. Appl. 12 (1977) 1487; B. Hird and S. P. Ali, Phys. Rev. Lett. 41 (1978) 540.
- 23) G. M. Raisbeck, F. Yiou and C. Stephen, J. Physique Lett. 40 (1979) L-241.
- 24) L. R. Kilus, R. P. Beukens, K. H. Chang, H. W. Lee, A. E. Litherland, D. Elmore, R. Ferraro and H. E. Gove, Nature 282 (1979) 488.
- 25) T. Lee, D. A. Papanastassiou and G. J. Wasserburg, Geophys. Res. Lett. 3 (1976) 109; and Astrophys. J. 211 (1977) L107.
- 26) J. W. Truran and A. G. W. Cameron, Astrophys. J. 219 (1978) 226.
- 27) W. D. Arnett and J. P. Wefel, Astrophys. J. 224 (1978) L139.

- 28) J. Heinemeier and P. Hvelplund, Nucl. Instrum. Methods 148 (1978) 425.
- 29) M. Paul, W. Henning, W. Kutschera, E. J. Stephenson and J. L. Yntema,
Phys. Lett. B. in press.
- 30) W. Kutschera, W. Henning, M. Paul, R. K. Smither, E. J. Stephenson,
J. L. Yntema, D. E. Alburger, J. B. Cumming and G. Harbottle,
Phys. Rev. Lett., in press.
- 31) Prepared by D. E. Alburger and G. Harbottle, Brookhaven National Laboratory,
Upton, New York 11973, U.S.A.
- 32) H. B. Clausen, J. of Glaciology 12 (1973) 411.
- 33) D. J. DeMaster, Earth and Plan. Sci. Lett. 48 (1980) 209.
- 34) R. N. Lewis, Nucl. Instrum. Methods 151 (1978) 371.
- 35) F. Ajzenberg-Selove, Nucl. Phys. A268 (1976) 61.
- 36) E. A. Samworth, E. K. Warburton and G. A. P. Engelbertink, Phys. Rev. C5
(1972) 138.
- 37) P. M. Endt and C. Van Der Leun, Nucl. Phys. A310 (1978) 424.
- 38) G. M. Raisbeck and F. Yiou, 20th Inst. Symp. for Archeometry, Paris,
March 26-29, 1980, to be published in Revue d' Archéométrie.

Radio-isotope	Half-life (yr)	Ref.	Isotope ratio	Origin of sample material	Isotope ratio (10^{-12}) measured by	
					Ion counting	Decay counting
^{14}C	5730 ± 40	35	$^{14}\text{C}/^{12}\text{C}$	Recent charcoal Maya charcoal "Fermi" graphite Graphite	1.06 ± 0.15 0.948 ± 0.095 4.5 ± 0.7 0.20 ± 0.05	$1.144 \pm 0.011^{\text{a}}$ $0.950 \pm 0.009^{\text{a}}$ $5.137 \pm 0.041^{\text{a}}$ not measured
^{26}Al	$(7.16 \pm 0.32) \times 10^5$	36	$^{26}\text{Al}/^{27}\text{Al}$	$^{27}\text{Al}(\gamma, n)^{26}\text{Al}$ $^{27}\text{Al}(\gamma, n)^{26}\text{Al}$ $^{27}\text{Al}(^{16}\text{O}, ^{17}\text{O})^{26}\text{Al}$ $^{26}\text{Mg}(p, n)^{26}\text{Al}$ $^{26}\text{Mg}(p, n)^{26}\text{Al}$ $^{26}\text{Mg}(p, n)^{26}\text{Al}$ $^{26}\text{Mg}(p, n)^{26}\text{Al}$ $^{26}\text{Mg}(p, n)^{26}\text{Al}$ $^{26}\text{Mg}(p, n)^{26}\text{Al}$ Blank	$290 \pm 60^{\text{b}}$ $650 \pm 80^{\text{b}}$ 91 ± 30 204 ± 26 136 ± 20 92 ± 13 85 ± 13 18 ± 6 < 4	$420 \pm 20^{\text{b}}$ $420 \pm 20^{\text{b}}$ not measured not measured not measured not measured not measured not measured not measured
^{32}Si	101 ± 18	30	$^{32}\text{Si}/\text{Si}$	$^{30}\text{Si}(t, p)^{32}\text{Si}$ $^{30}\text{Si}(^{18}\text{O}, ^{16}\text{O})^{32}\text{Si}$	28200 ± 5000 0.095 ± 0.050	c) not measured
^{36}Cl	$(3.01 \pm 0.02) \times 10^5$	37	$^{36}\text{Cl}/\text{Cl}$	$^{35}\text{Cl}(n, \gamma)^{36}\text{Cl}$ $^{35}\text{Cl}(n, \gamma)^{36}\text{Cl}$ $^{35}\text{Cl}(n, \gamma)^{36}\text{Cl}$ $^{35}\text{Cl}(n, \gamma)^{36}\text{Cl}$ NaCl, blank	14900 ± 2200 1360 ± 200 100 ± 20 60 ± 20	$12900 \pm 700^{\text{d}}$ $1450 \pm 100^{\text{d}}$ 36.8 ± 2.0

a) Measured from β activity with samples from the same material by D. D. Coleman, Illinois State Geological Survey, Urbana, Illinois, U.S.A.

b) See also table II and sec. 3.2.

c) Half-life measurement of ^{32}Si . See sec. 3.3 and ref. 30.

d) Not from ^{36}Cl decay. See sec. 3.4.

Table II

Typical running conditions of the Argonne FN Tandem for mass spectroscopy measurements of different radioisotopes.

Isotope	Source Material	Radioisotope Production and Concentration	$i_{LE}^{(a)}$ (nA)	Terminal Voltage Readings (MV)	$i_{HE}^{(b)}$ (nA)	Analyzed Charge State	$i_{Shutter}^{(c)}$ (nA)	$i_{Target}^{(d)}$ (nA)	Spectrograph Charge State	Radio-isotope Count Rate (sec ⁻¹)
¹³ C	Graphite	- (n,γ)	24.0	6.425	44.0	4 ⁺	7.1	5.0		
¹⁴ C		4.5 × 10 ⁻¹²	0.50	5.964	0.80	4 ⁺	~ 0	~ 0	6 ⁺	1.9
²⁷ Al	Al	- (γ,n)	1.5	7.682	2.25	8 ⁺	0.75	0.52		
²⁸ Al		4.2 × 10 ⁻¹⁰	3.8	7.985	5.0	8 ⁺	~ 0	~ 0	11 ⁺	0.15
²⁹ Si	K ₂ SiF ₆	- (t,p)	3.0	6.979	6.6	9 ⁺	0.48	0.30		
³⁰ Si		2.8 × 10 ⁻⁸	14.0	7.990	17.0	9 ⁺	0.28	0.21	9 ⁺	0.51
³⁵ Cl	NaCl	- (n,γ)	29.0	7.791	45	10 ⁺	1.37	0.83		
³⁶ Cl		1.4 × 10 ⁻⁹	21.5	8.000	~ 0	10 ⁺	~ 0	~ 0	13 ⁺	0.79

36

Intensity of the negative ion beam injected into the accelerator, as measured at the Faraday cup after the 40° injection magnet (see Fig. 1). In most cases molecular background components are admixed (e.g. ¹²CH⁻, ¹²CH₂⁻, ¹³CH⁻, CN⁻, ¹⁶O₂⁻, C₃⁻).

Total charge current of the positive ion beam as measured at the Faraday cup after the accelerator.

Total charge current of the analyzed beam of given charge state measured after the 90° magnet.

Total charge current of the analyzed beam measured at the target position of the split-pole spectrograph.

Table III

Results of the $^{26}\text{Mg}(p,n)^{26}\text{Al}$ (7.2×10^5 yr) cross section measurements

$E_{\text{c.m.}}^p$ = center-of-mass proton energy (± 0.1 MeV due to target thickness); T = collecting time of $^{26}\text{Al}^{11+}$ ions; $N(^{26}\text{Al}^{11+})$ = number of $^{26}\text{Al}^{11+}$ counts; $I(^{27}\text{Al}^{8+})$ = average $^{27}\text{Al}^{8+}$ beam current. The cross section σ is calculated from the known quantities involved in the sample preparation and the $^{26}\text{Al}/^{27}\text{Al}$ ratio. The main contributions to the errors arise from statistics and the $^{27}\text{Al}^{8+}$ current measurements ($\leq 10\%$).

Sample #	$E_{\text{c.m.}}^p$ (MeV)	T (min)	$N(^{26}\text{Al}^{11+})$ (counts)	$I(^{27}\text{Al}^{8+})$ (nA)	$^{26}\text{Al}/^{27}\text{Al}$ (10^{-11})	σ (mb)
1	5.0	68	11	0.39	1.8 ± 0.6	7.4 ± 2.5
2	5.5	100	74	0.37	8.5 ± 1.3	37.3 ± 6.3
3	6.0	102	102	0.47	9.2 ± 1.3	28.2 ± 4.5
4	6.4	51	92	0.57	13.6 ± 2.0	42.6 ± 6.9
5	6.7	67	172	0.54	20.4 ± 2.6	65.2 ± 9.4
6	non-irradiated	33	0	0.32	< 0.4	

Table IV

Isotopic abundance for $^{28,29,30}\text{Si}$ as determined from relative beam current measurements with Si^{7+} ions at terminal voltage settings of 6.985, 7.225 and 7.485 MV, respectively.

Sample	Isotopic abundance (%)		
	^{28}Si	^{29}Si	^{30}Si
Natural Si abundance	92.23	4.67	3.10
$\text{K}_2^{\text{nat}}\text{SiF}_6$	92.23	4.97	2.80
$\text{K}_2^{32}\text{SiF}_6$	90.06	4.24	5.70
$\text{K}_2^{30}\text{SiF}_6$	4.42	0.43	95.15
Enriched ^{30}Si as quoted	3.78	0.67	95.55

Figure Captions

- Fig. 1. Schematic layout of the Argonne FN tandem accelerator and the experimental system used in the radioisotope-detection measurements.
- Fig. 2. The inverted Cs-beam sputter source¹²⁾.
- Fig. 3. Typical sample mount in the inverted sputter source.
- Fig. 4. Split-pole magnetic spectrograph¹⁴⁾.
- Fig. 5. Cross section of the focal-plane detector¹⁵⁾.
- Fig. 6. Example for typical charge and mass resolution as obtained with the split-pole focal-plane detector. Two-dimensional density plots for various reaction products from the reaction $^{18}\text{O} + ^{40}\text{Ca}$ at 56 MeV incident ^{18}O -beam energy.
- Fig. 7. Schematic illustration of a ^{36}Cl measurement with the energy-loss dispersion method. Additional negative-ion background components of appreciable intensity which are not shown in the figure are $^{18}\text{O}_2^-$ and $^{12}\text{C}_3^-$.
- Fig. 8. Focal-plane position spectra of $^{36}\text{Cl}^{13+}$ and $^{36}\text{S}^{13+}$ ions after passage of an 88-MeV incident $^{36}\text{S} + ^{36}\text{Cl}$ beam through different absorber foils. The ions originate from a NaCl sample with $^{36}\text{Cl}/\text{Cl} \approx 10^{-8}$.
- Fig. 9. Energy-loss straggling of 72-MeV ^{28}Si ions in various foils. (a) Ratio of the experimentally observed full straggling width at half maximum, $\delta E_{1/2}$, to the mean energy loss $\overline{\Delta E}$, as a function of $\overline{\Delta E}$. (b) Ratio of the measured straggling widths $\delta E_{1/2}(\text{exp})$ to theoretical values $\delta E_{1/2}(\text{calc})$, as calculated with

the expression given in ref. ²⁰). Foil thicknesses are given in $\mu\text{g}/\text{cm}^2$. Where foil stacks were used, the number of foils and their individual thicknesses are listed.

- Fig. 10. Reduced energy-loss straggling width, $\delta E_{\frac{1}{2}}^0$ (defined as α_{red} in ref. ²⁰) for various ions between ^{27}Al and ^{37}Al at 80 MeV incident energy on the aluminum foil stack ($15 \times 100 \mu\text{g}/\text{cm}^2$) versus mean energy loss in the foil, $\overline{\Delta E}$. The solid line is the prediction calculated from the empirical relation given in ref. ²⁰). The dashed line is a hand-drawn average through the data points.
- Fig. 11. ^{14}C yield from the "Fermi" graphite (table I) as a function of terminal voltage and injection magnet field setting, respectively.
- Fig. 12. Contour plot of the total energy, E_{total} , versus differential energy loss, ΔE , as obtained with the split-pole focal plane detector for the recent charcoal sample (table I). The ^{14}C counting rate was 25 per minute. The vertical scale is linear. ^{13}C is about 10 times and ^{12}C about two times stronger than ^{14}C .
- Fig. 13. Contour plot of the total energy, E_{total} , versus differential energy loss, ΔE , measured with the split-pole focal-plane detector for two ^{26}Al samples (see tables I and III). Sample #3 shows a clearly separated $^{26}\text{Al}^{11+}$ peak, whereas zero $^{26}\text{Al}^{11+}$ counts are observed for the non-irradiated sample #6. The inserts to the left are projections onto the E_{total} vs. ΔE plane. The vertical scale of the contour plots is linear

and the same for both samples. The ^{27}Al and ^{26}Mg background peaks of sample #3 are about 10 times stronger than the ^{26}Al peak.

Fig. 14. Two-dimensional density plots of the total energy, E_{total} , versus differential energy loss, ΔE , measured with the split-pole focal plane detector for: (a) a K_2SiF_6 sample containing ^{32}Si and (b) a blank sample. The indicated sections are plotted in fig. 15 in a contour-type plot.

Fig. 15. Contour plot of the differential energy loss, ΔE , versus total energy signals, E_{total} , in the focal plane detector for ions measured at $\theta_{\text{lab}} = 0^\circ$ from an active K_2SiF_6 sample (700 $^{32}\text{Si}^{9+}$ counts in 20 min) and an inactive K_2SiF_6 sample (zero $^{32}\text{Si}^{9+}$ counts in 11 min, $^{32}\text{Si}/\text{Si} < 1 \times 10^{-10}$). The $^{27}\text{Al}^{9+}$ background counts are produced by elastic scattering of the ^{32}S beam from Al foil stack nuclei. The vertical scale of the contour plot is linear and the same for both spectra.

Fig. 16. Focal-plane position spectra for various stages of the detection of ^{32}Si . (a) Scattered ^{32}S background spectrum at $\theta_{\text{lab}} = 3^\circ$. (b) Spectrum at $\theta_{\text{lab}} = 0^\circ$ which falls on the slit in the tantalum shield. (c) ^{32}Si component in this spectrum which is obtained by gating on ^{32}Si in the ΔE vs. E_{total} spectrum (figs. 14 and 15).

Fig. 17. Summary of $^{32}\text{Si}/\text{Si}$ ratio measurements. Errors are statistical only. The three runs refer to measurements performed several months apart. The unweighted mean is indicated by the solid line. The dashed lines give the extend of the systematic error discussed in the text.

Fig. 18. (a) Position ($B\rho$) spectrum from an NaCl sample with $^{36}\text{Cl}/\text{Cl} \approx 10^{-8}$ as measured in the focal-plane detector of the spectrograph, gated by the Cl plus S group in the ΔE -E spectrum. (b) Position spectrum with an additional window set on $^{36}\text{Cl}^{13+}$ in the E vs $B\rho$ spectrum (fig. 19).

Fig. 19. ΔE vs E and E vs $B\rho$ spectra for the same ^{36}Cl sample as in fig. 18.

Fig. 20. Preliminary results of a test to use the superconducting post accelerator at Argonne for accelerator mass spectrometry. (a) Calculated range differences between ^{32}Si and ^{32}S ions in different absorber materials. (b) Ion yield measured in a ΔE /E surface barrier detector telescope after the linac, for a sample with no ^{32}Si (dashed curve) and a sample containing ^{32}Si with a $^{32}\text{Si}/\text{Si}$ ratio of approximately 10^{-8} .

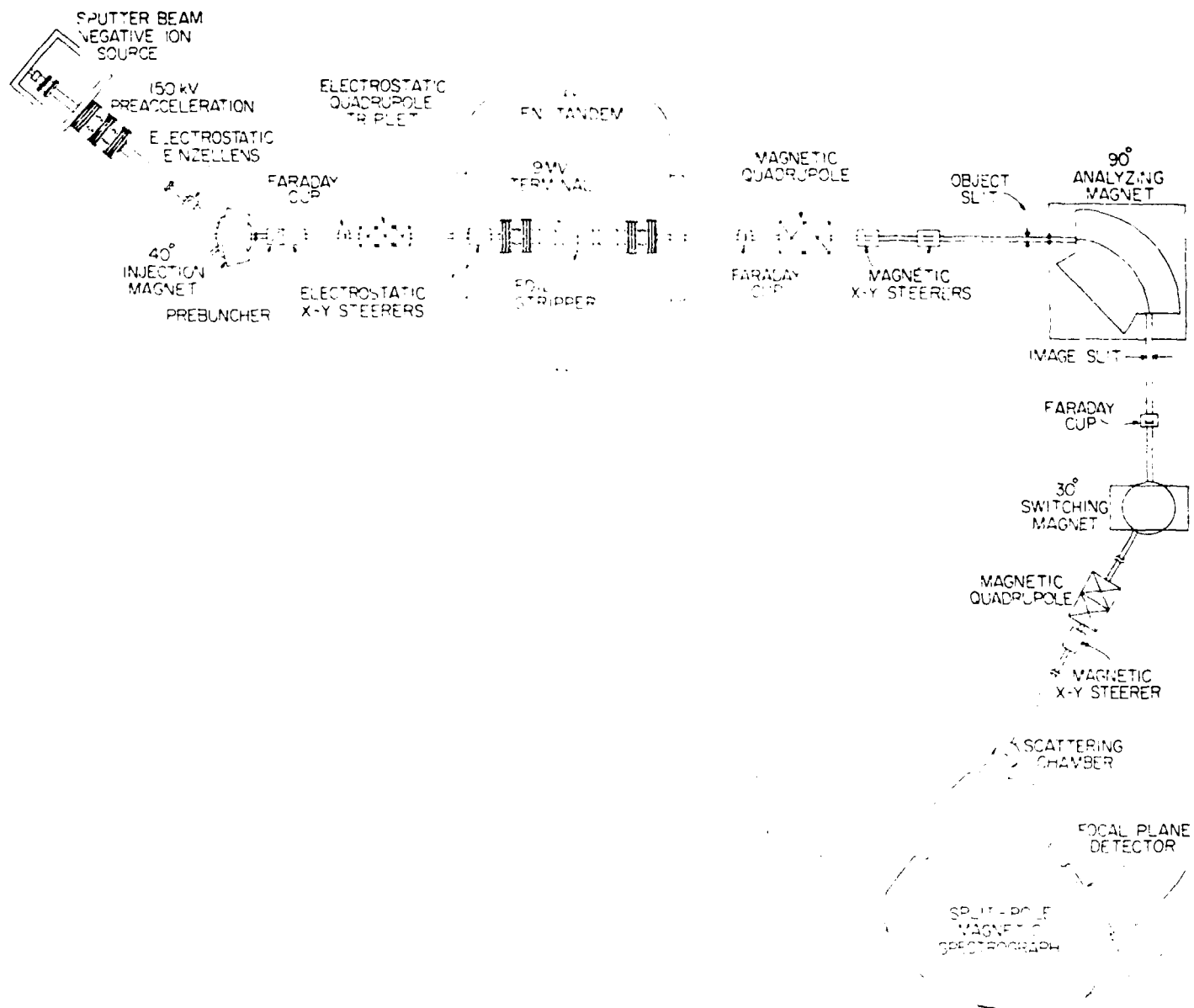
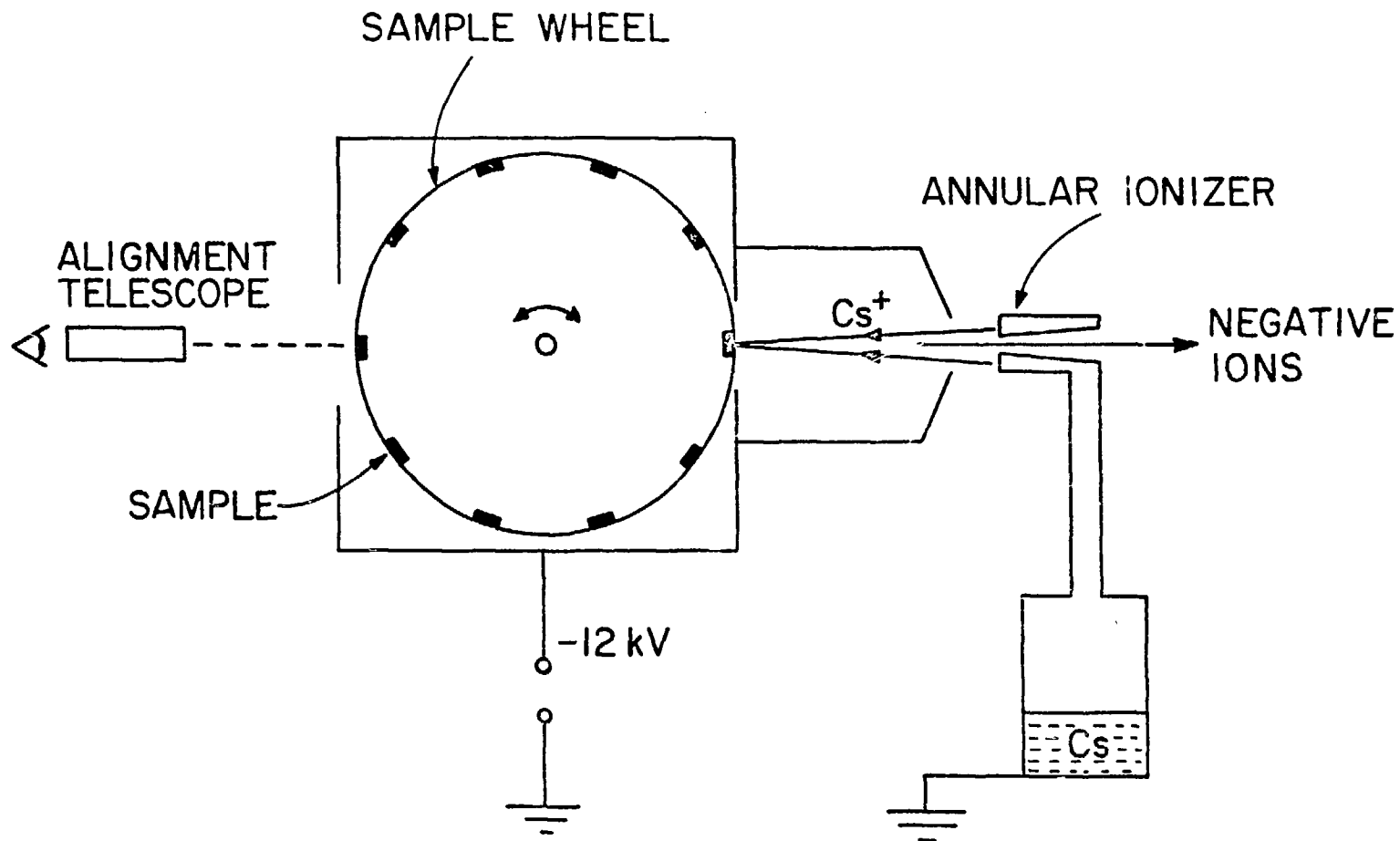
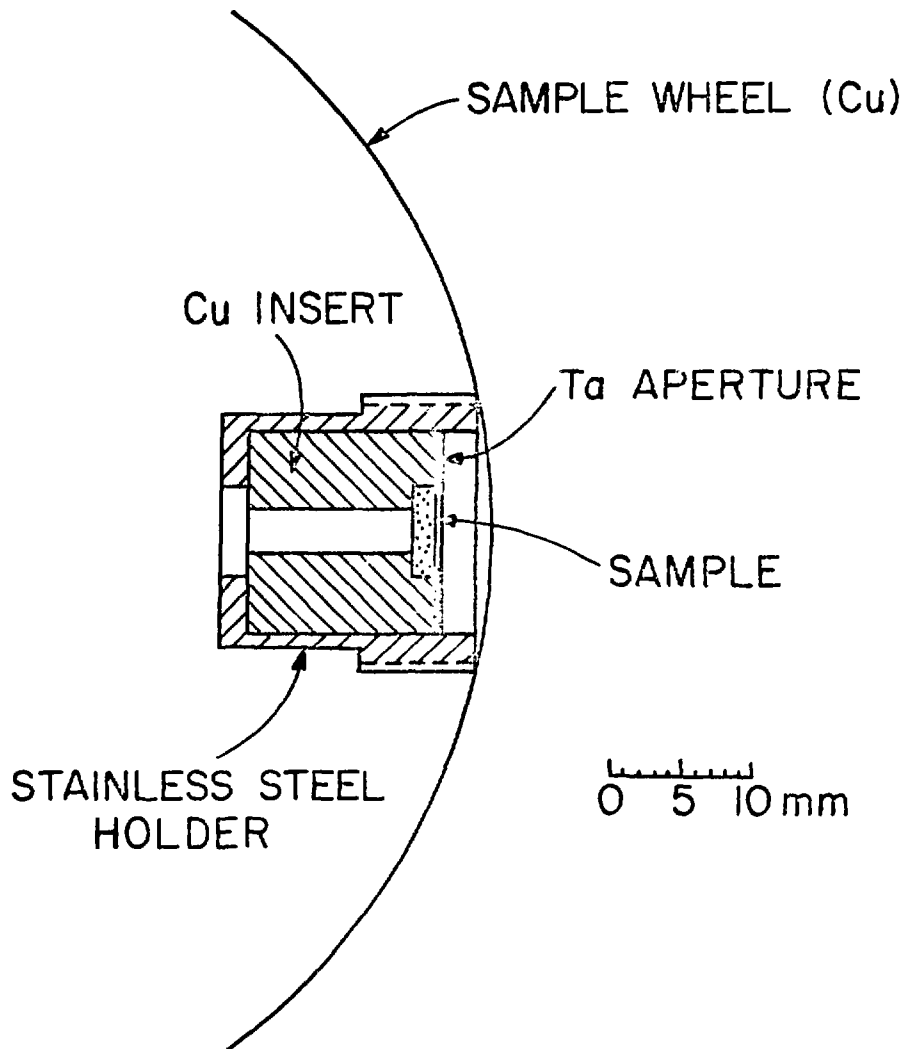


Fig. 1



SCHEMATIC VIEW OF THE INVERTED SPUTTER SOURCE

PHG-15,804



SPUTTER SAMPLE GEOMETRY

SPLIT-POLE MAGNETIC SPECTROGRAPH

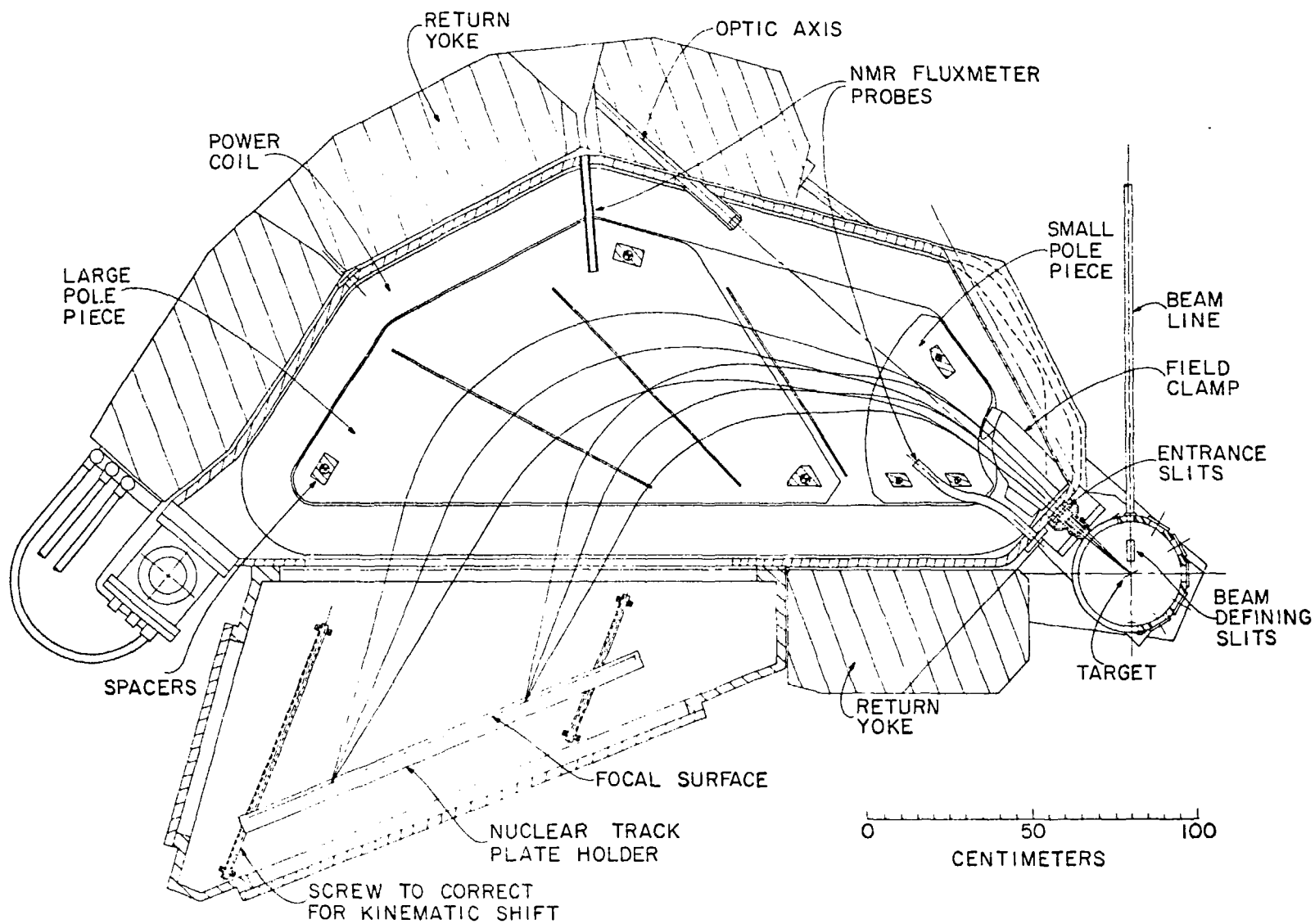
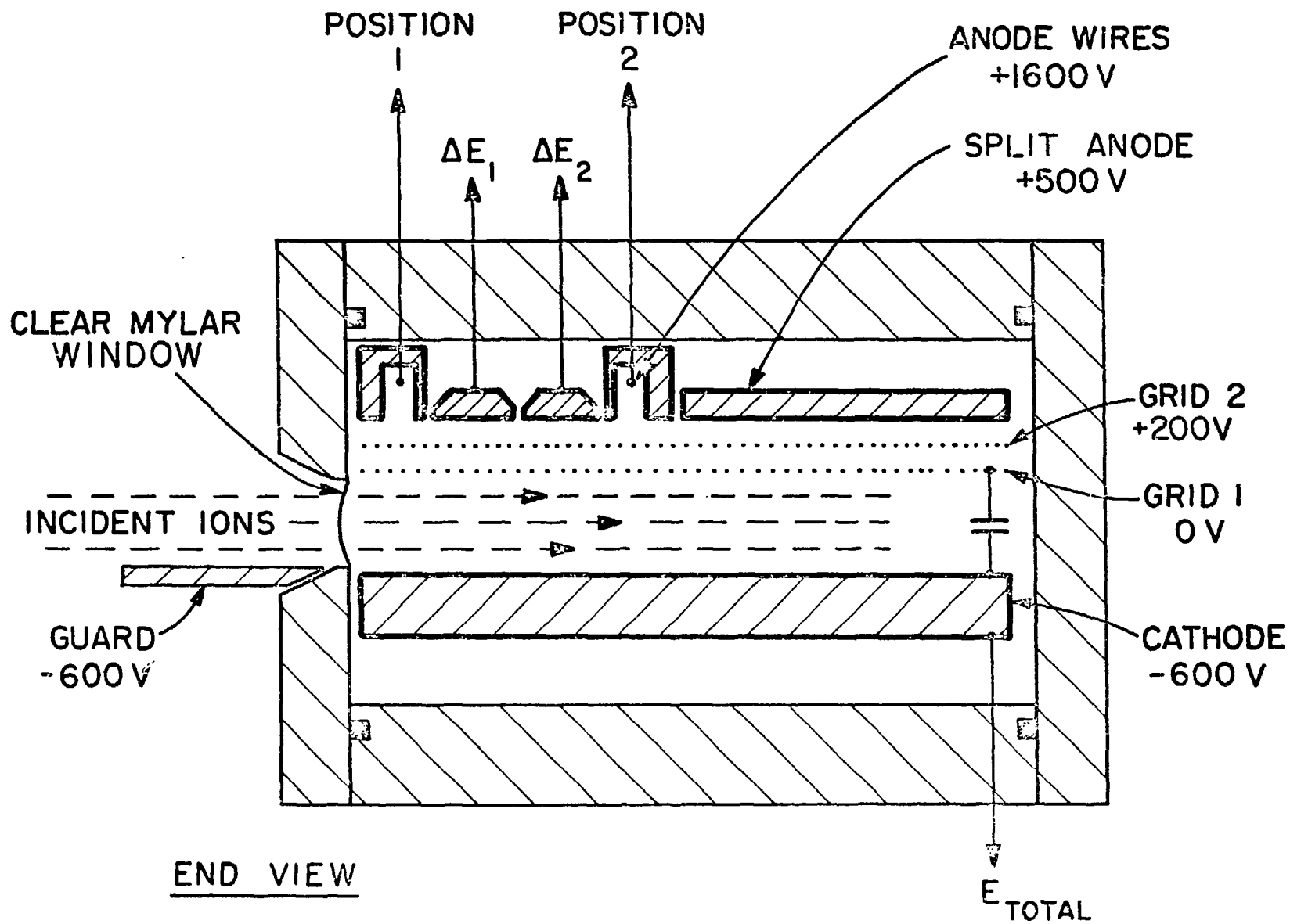
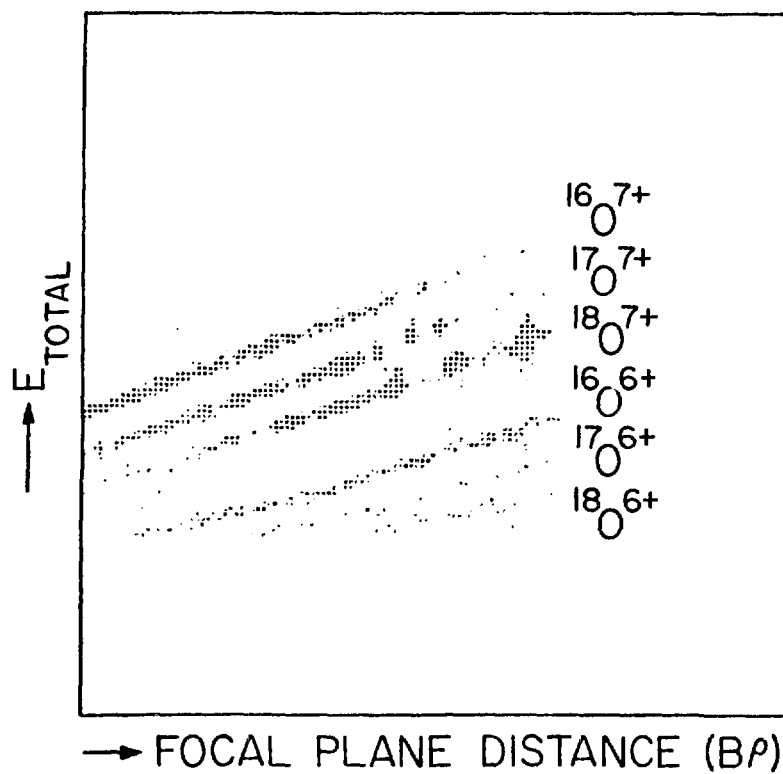
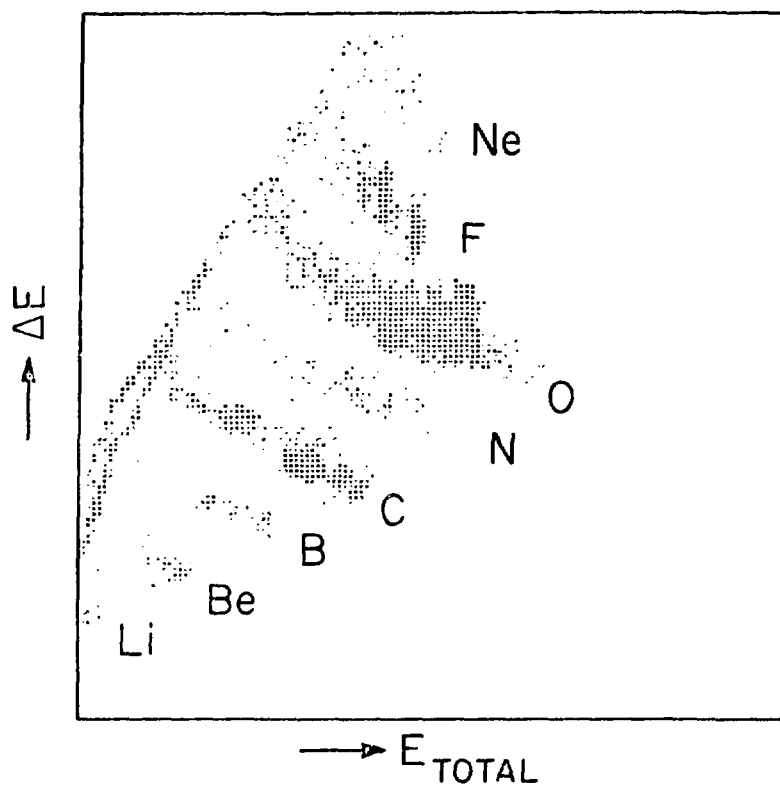
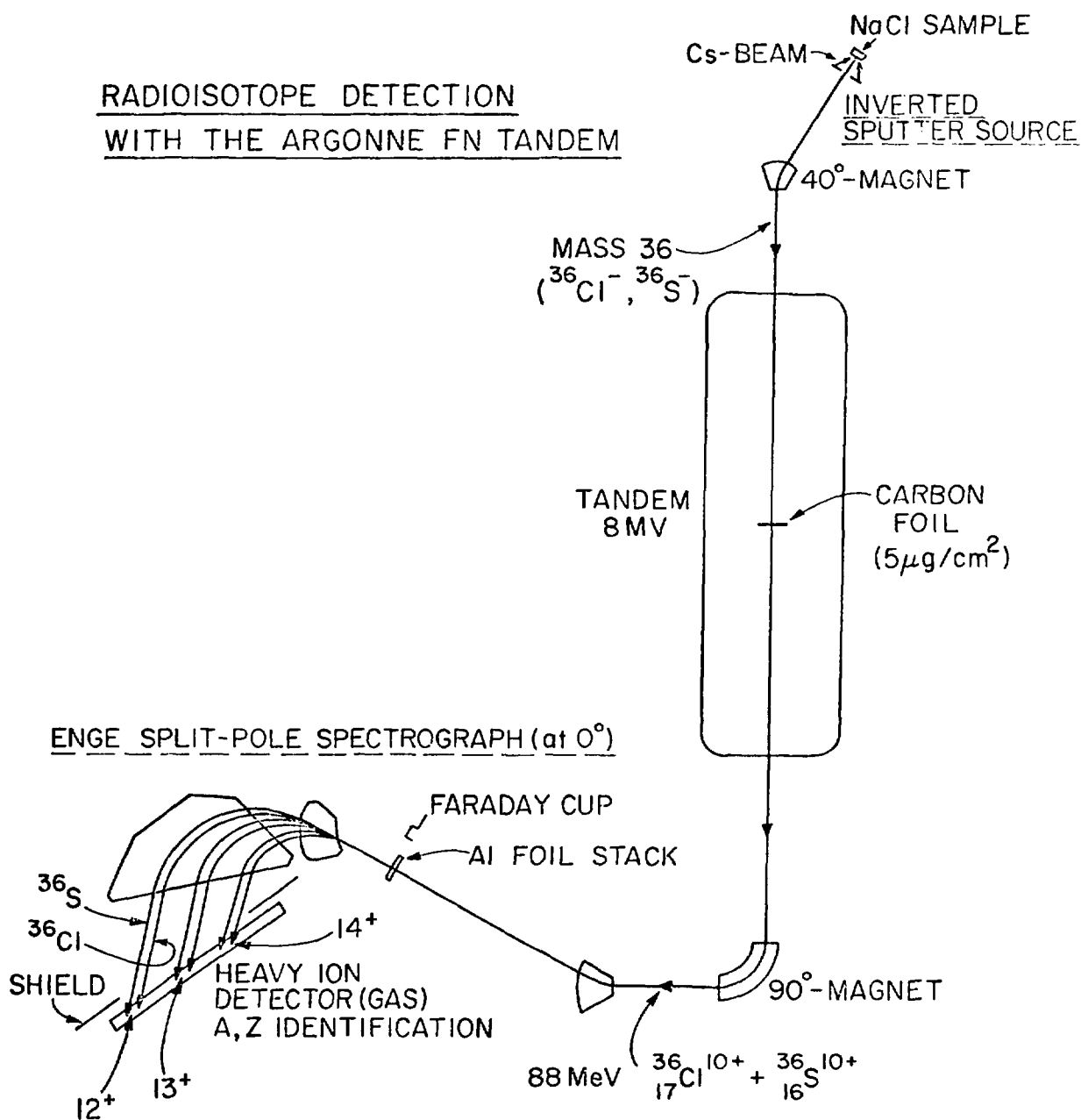


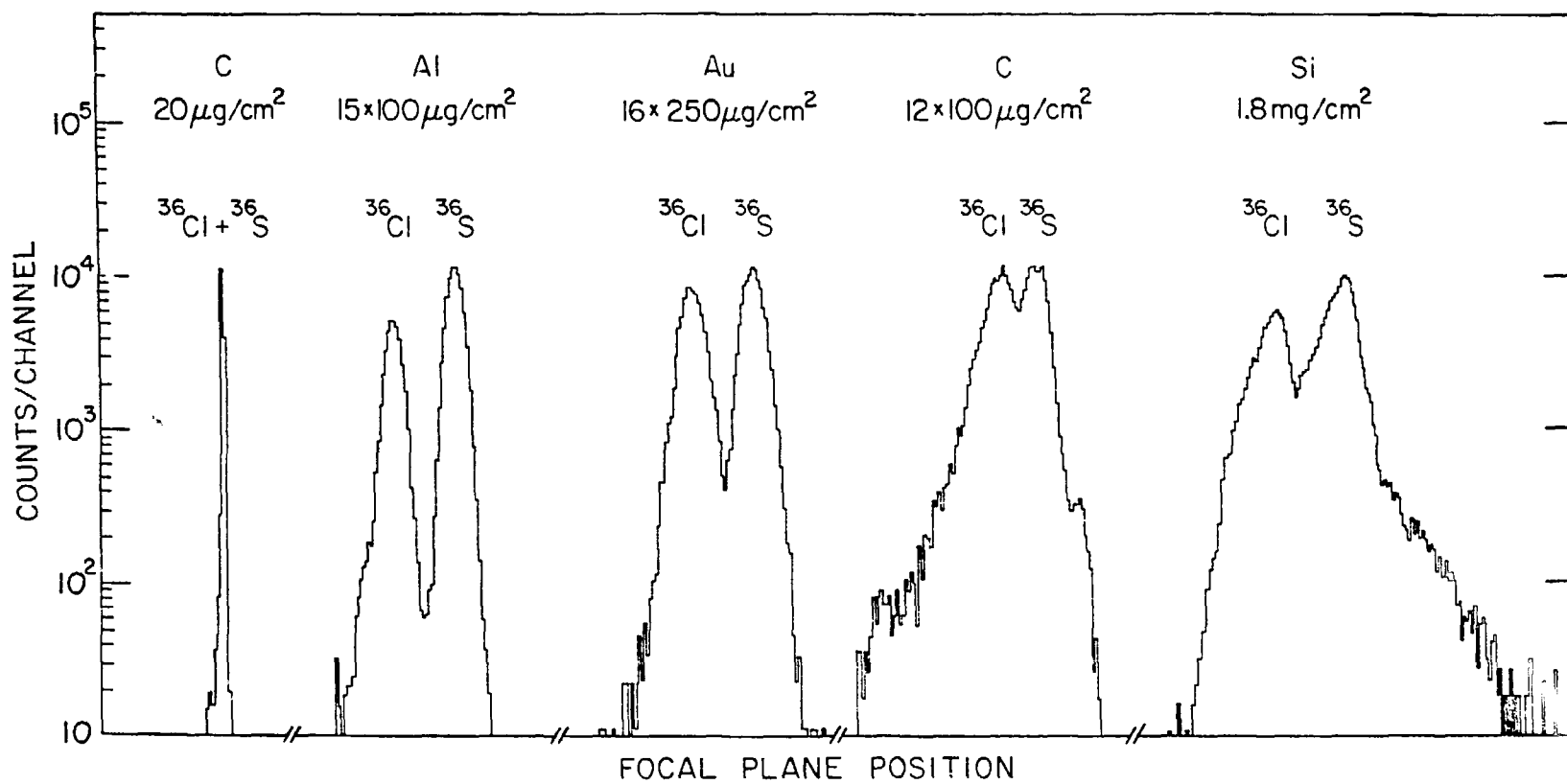
Fig. 4

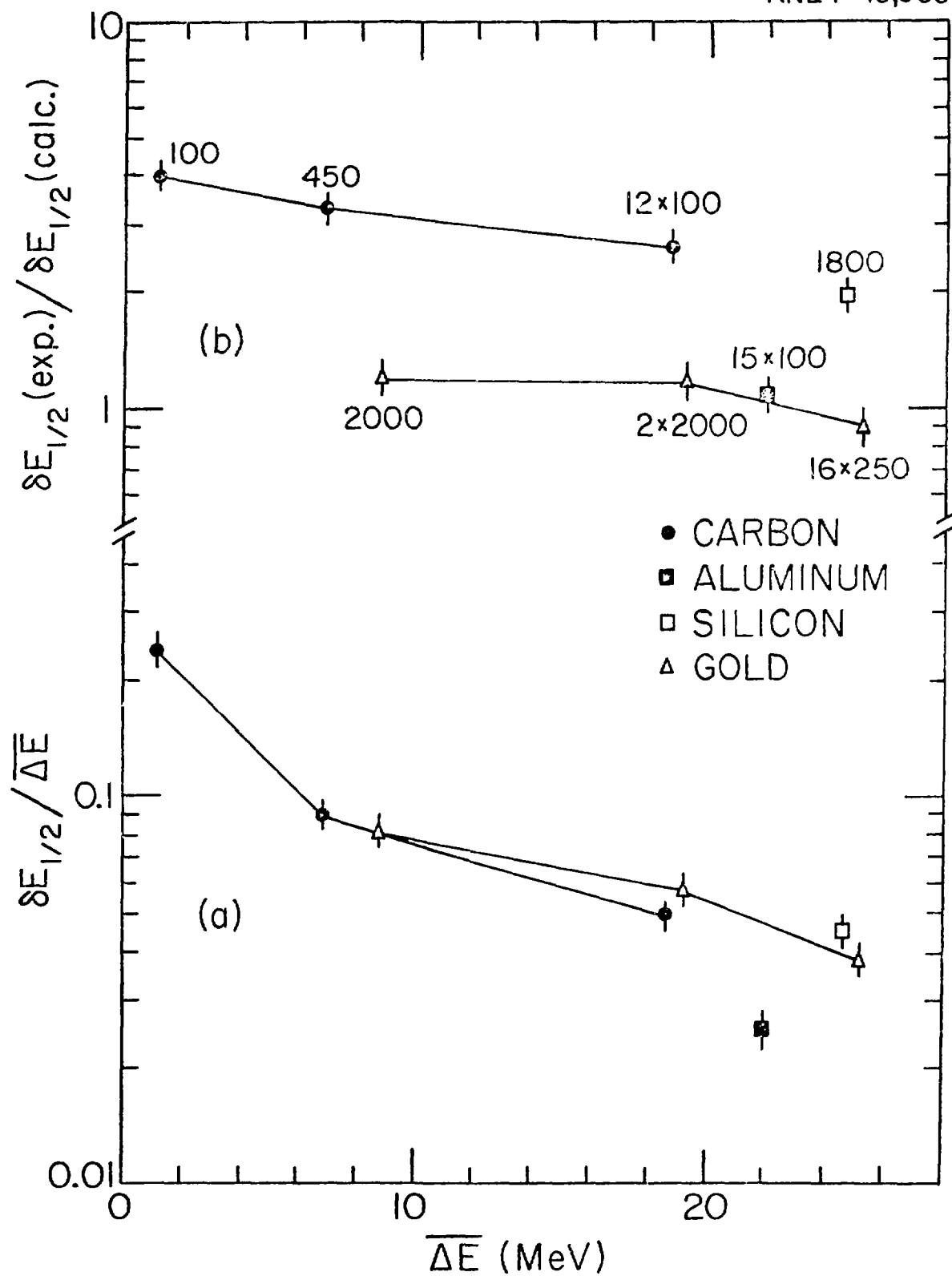


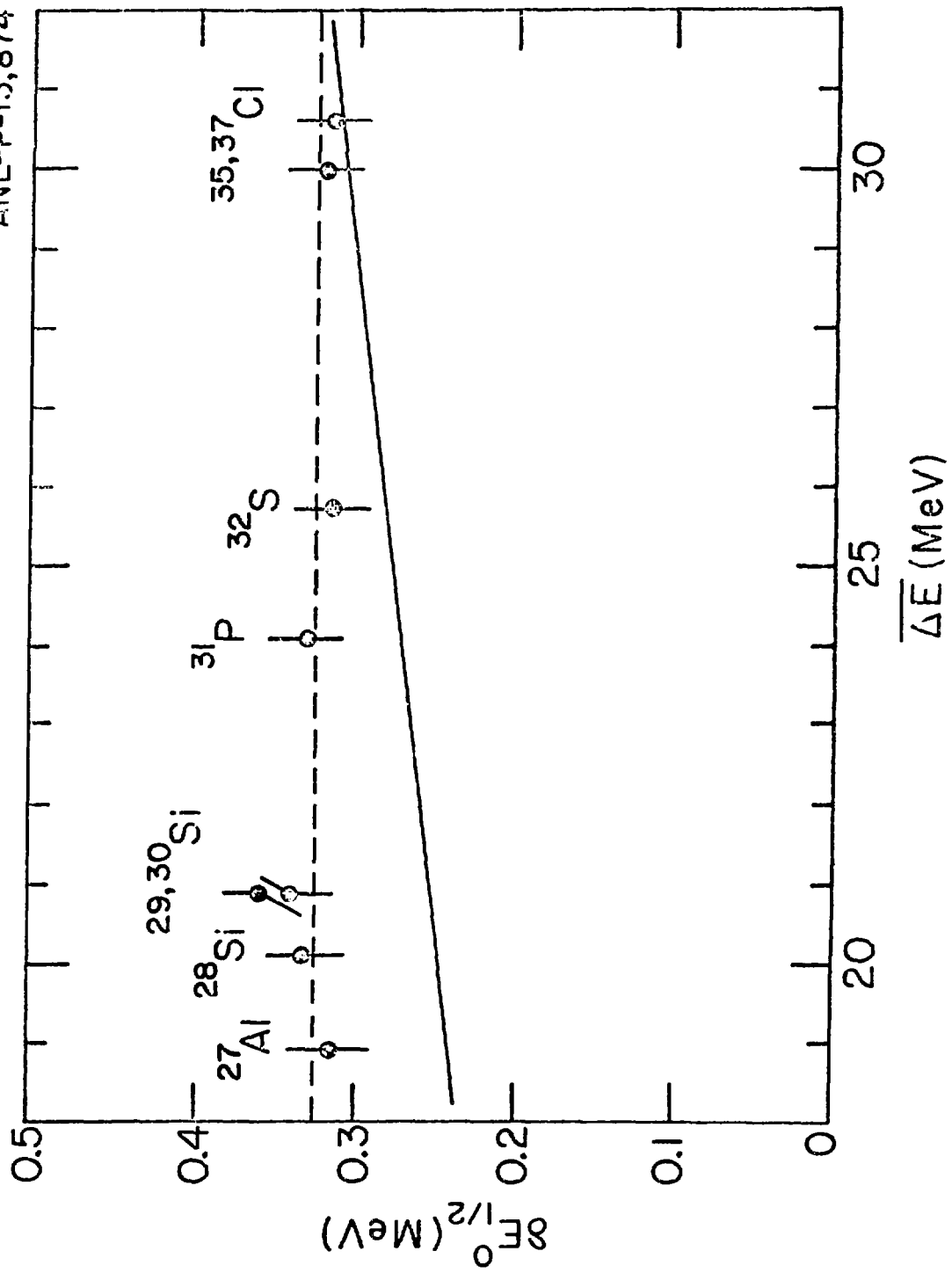


RADIOISOTOPE DETECTION WITH THE ARGONNE FN TANDEM

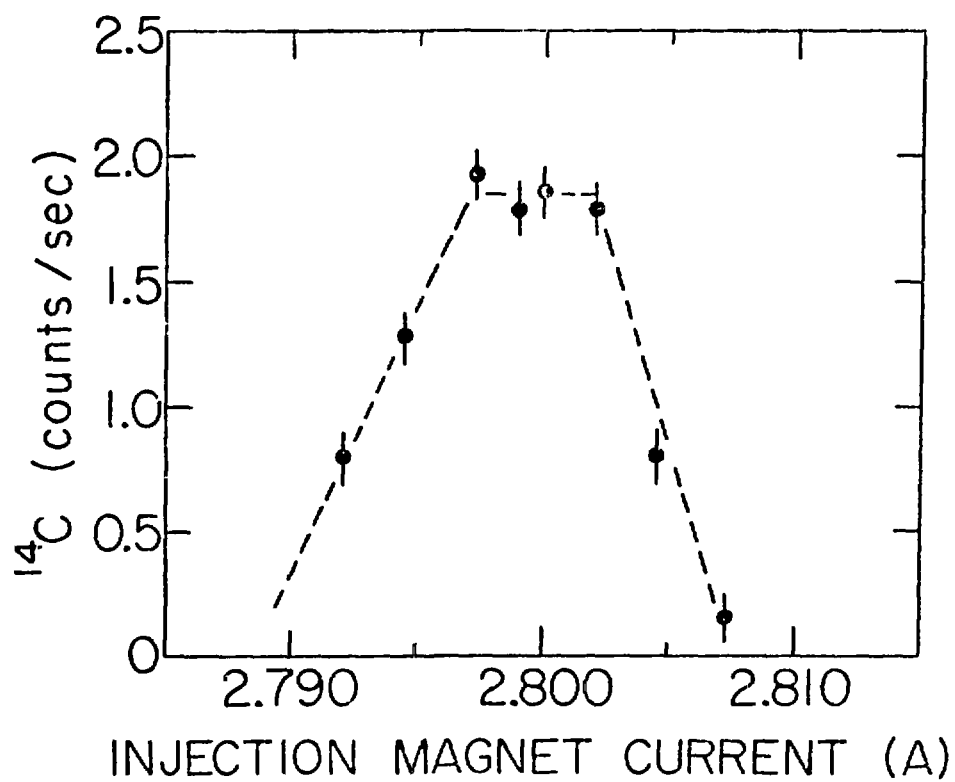
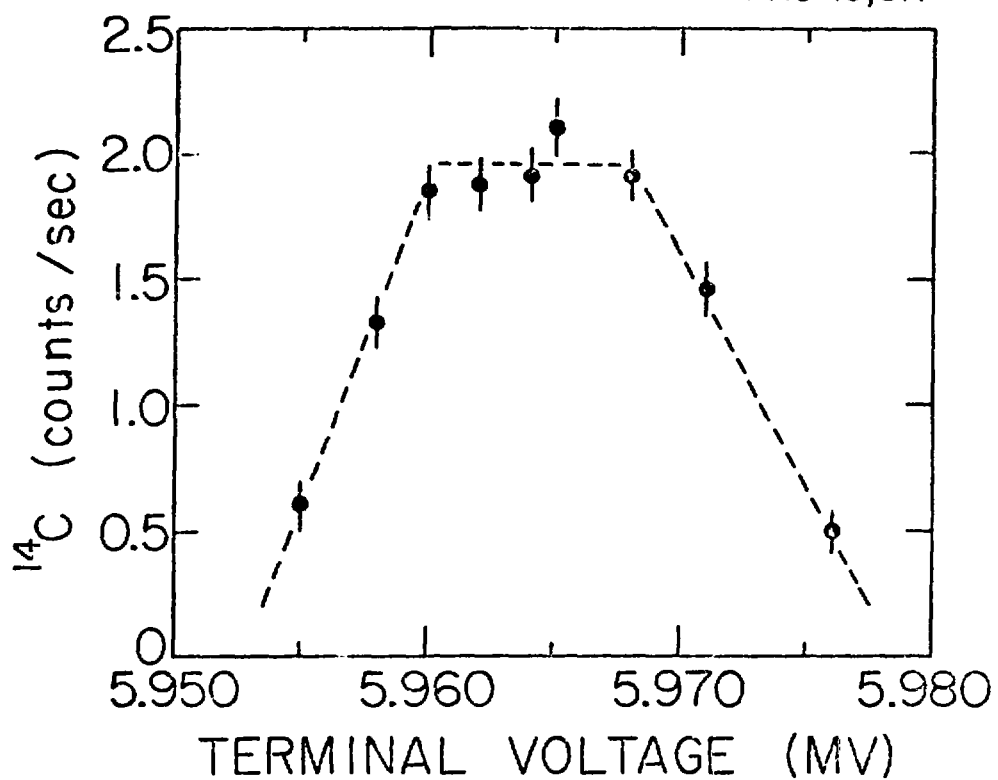








PHG-15,817



ANL-P-15,875

RECENT CHARCOAL SAMPLE

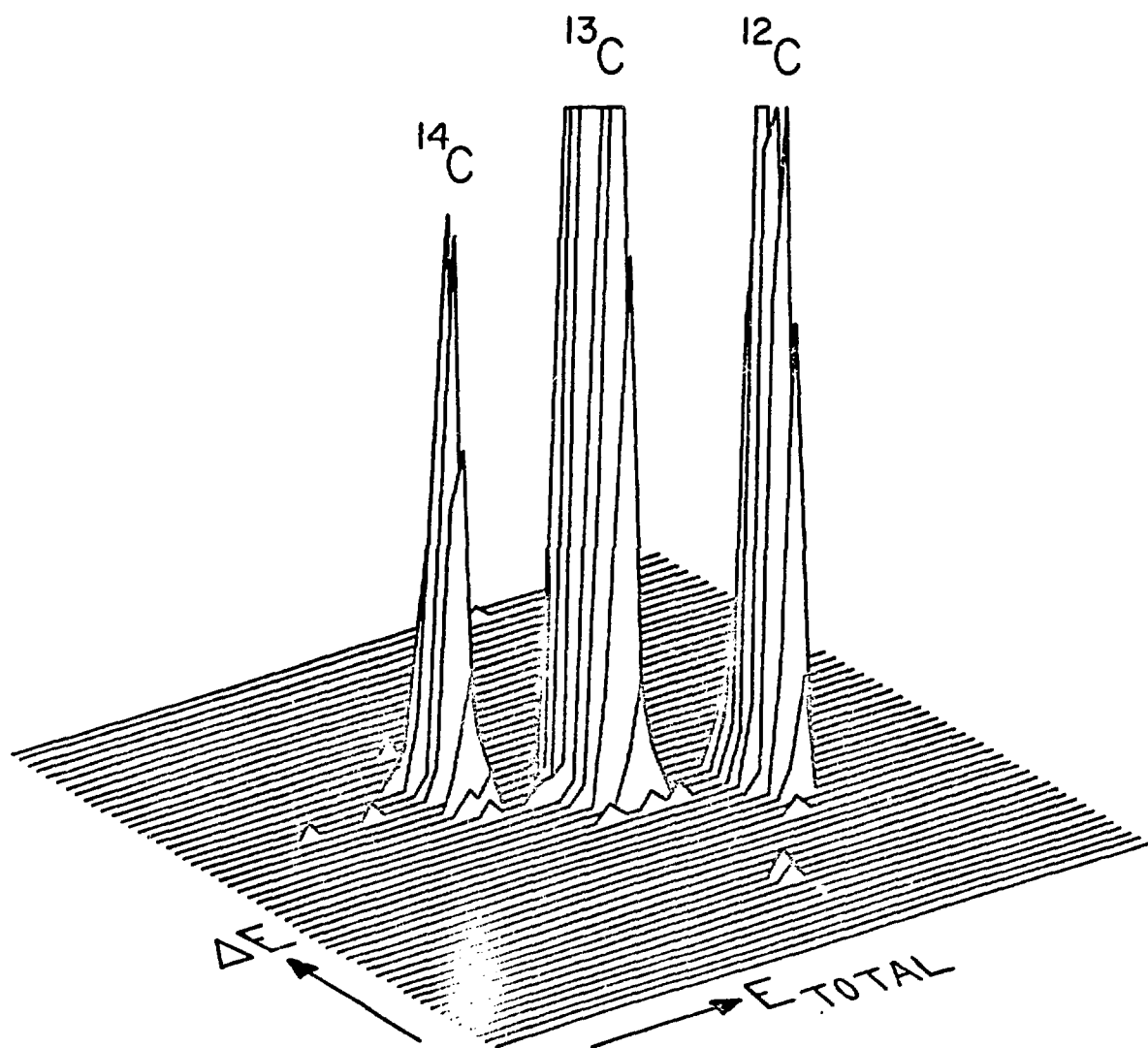


Fig. 12

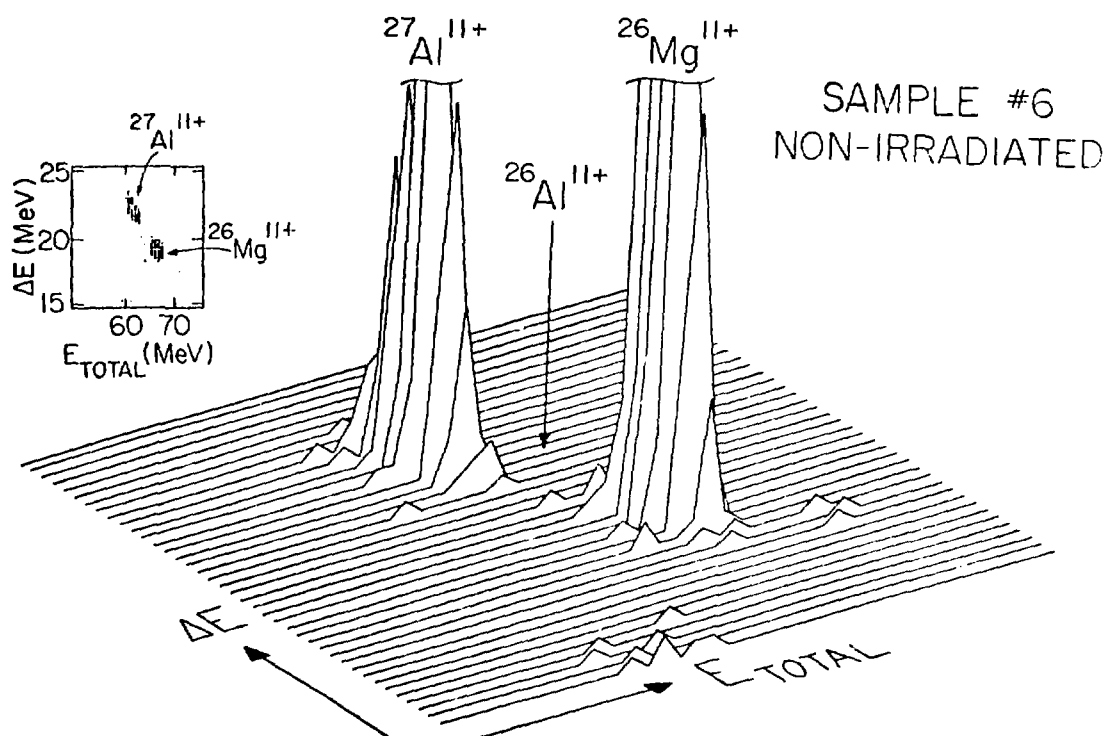
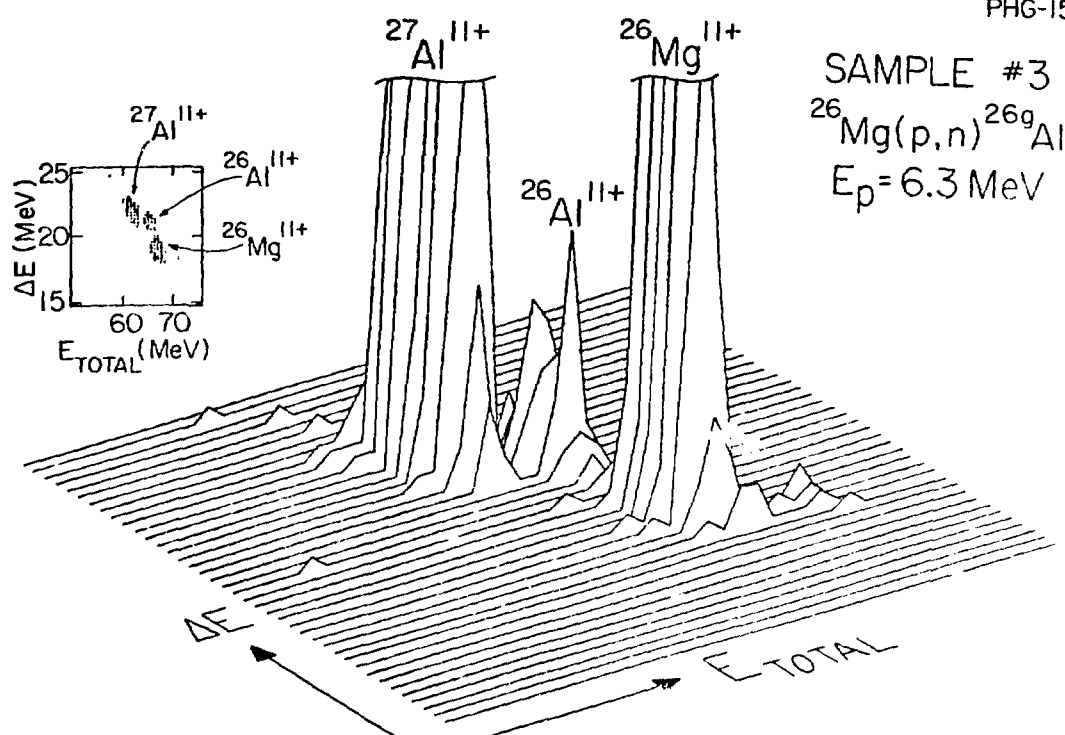
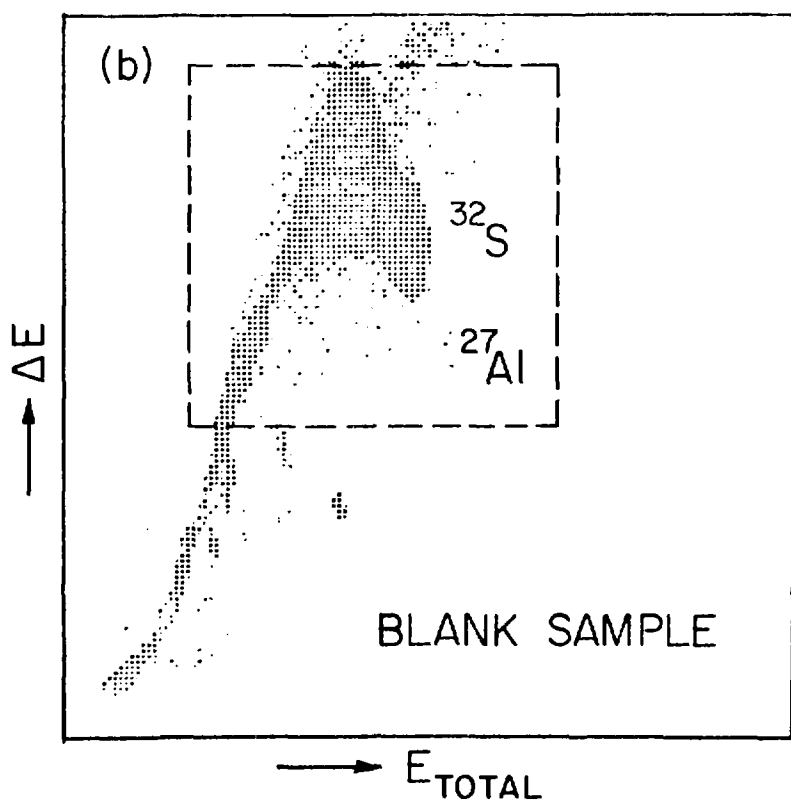
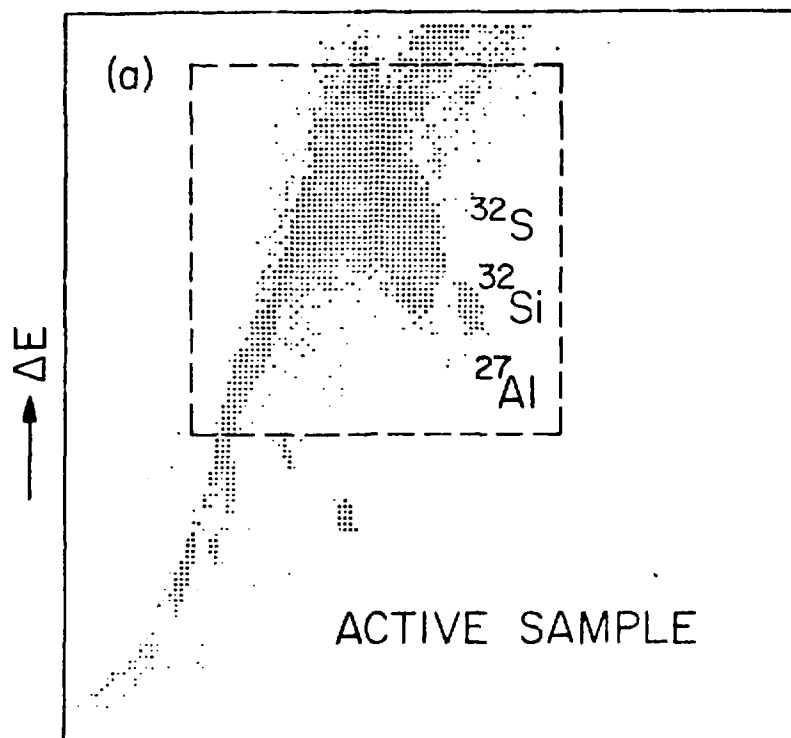
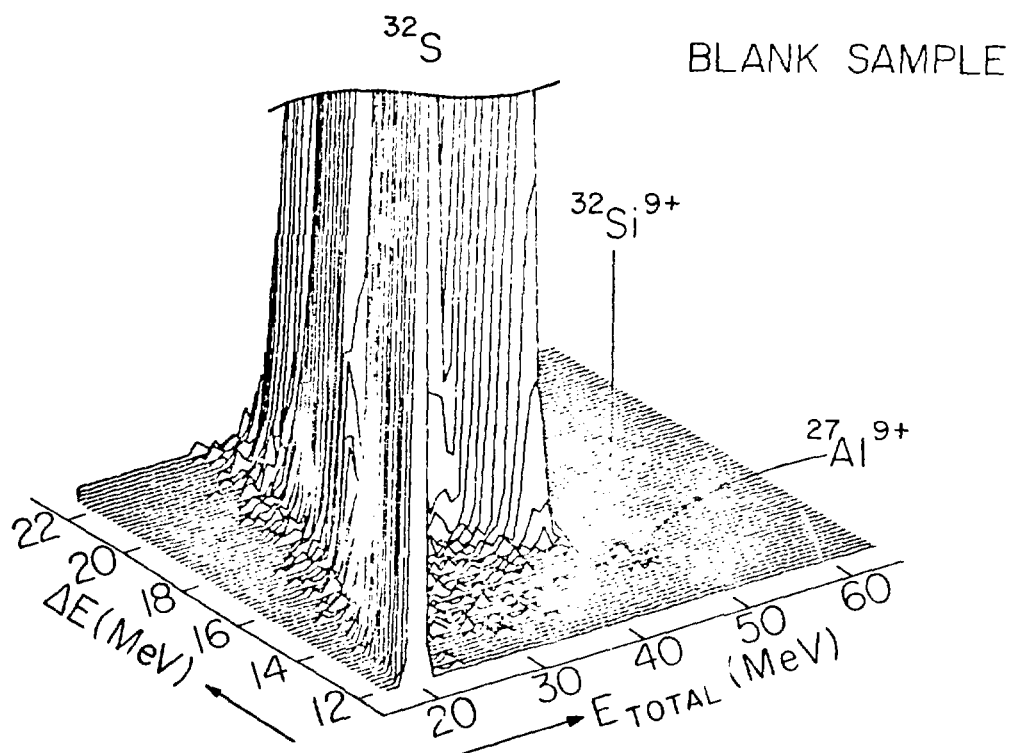
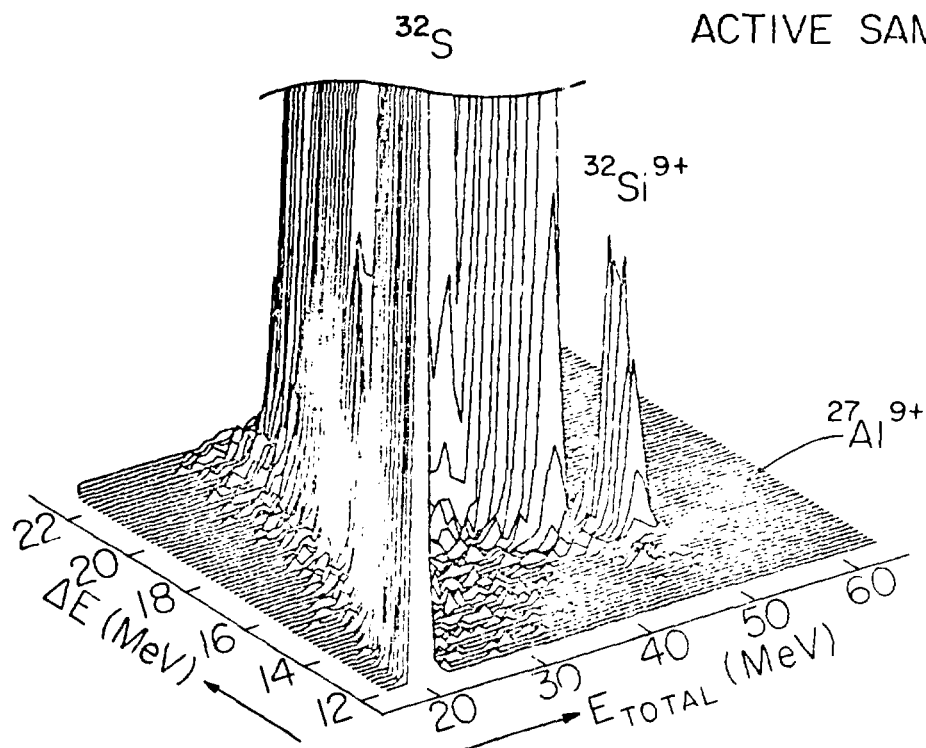
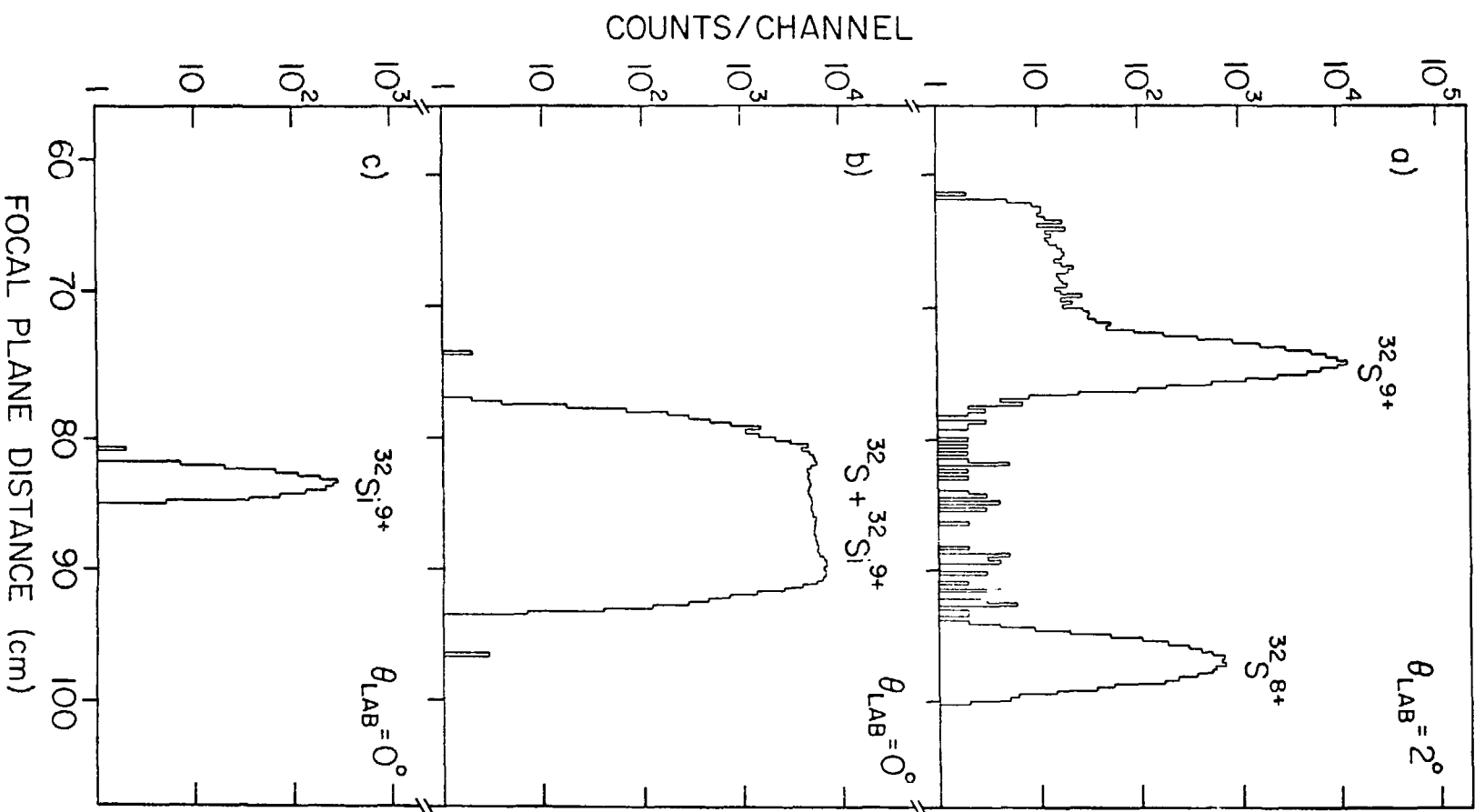


FIG. 13







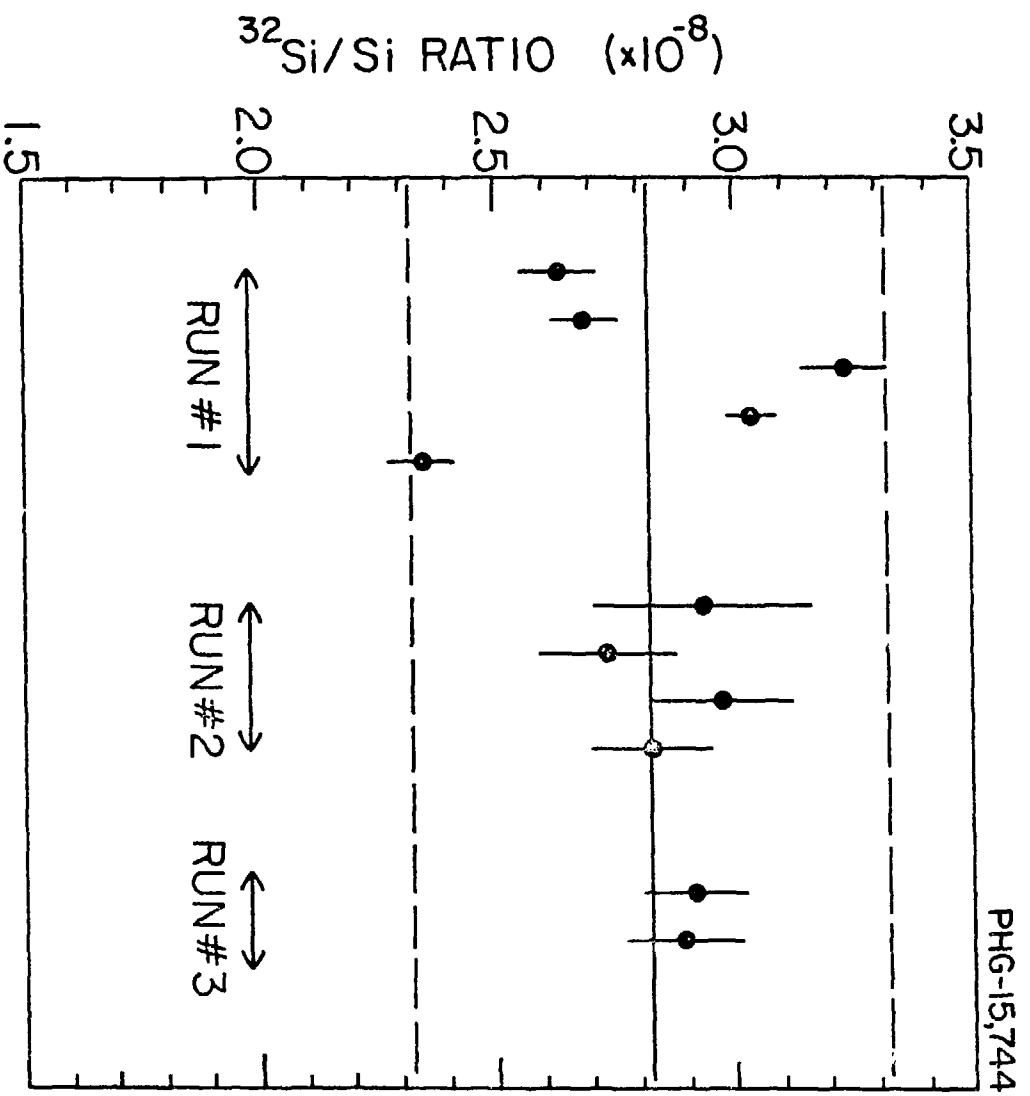
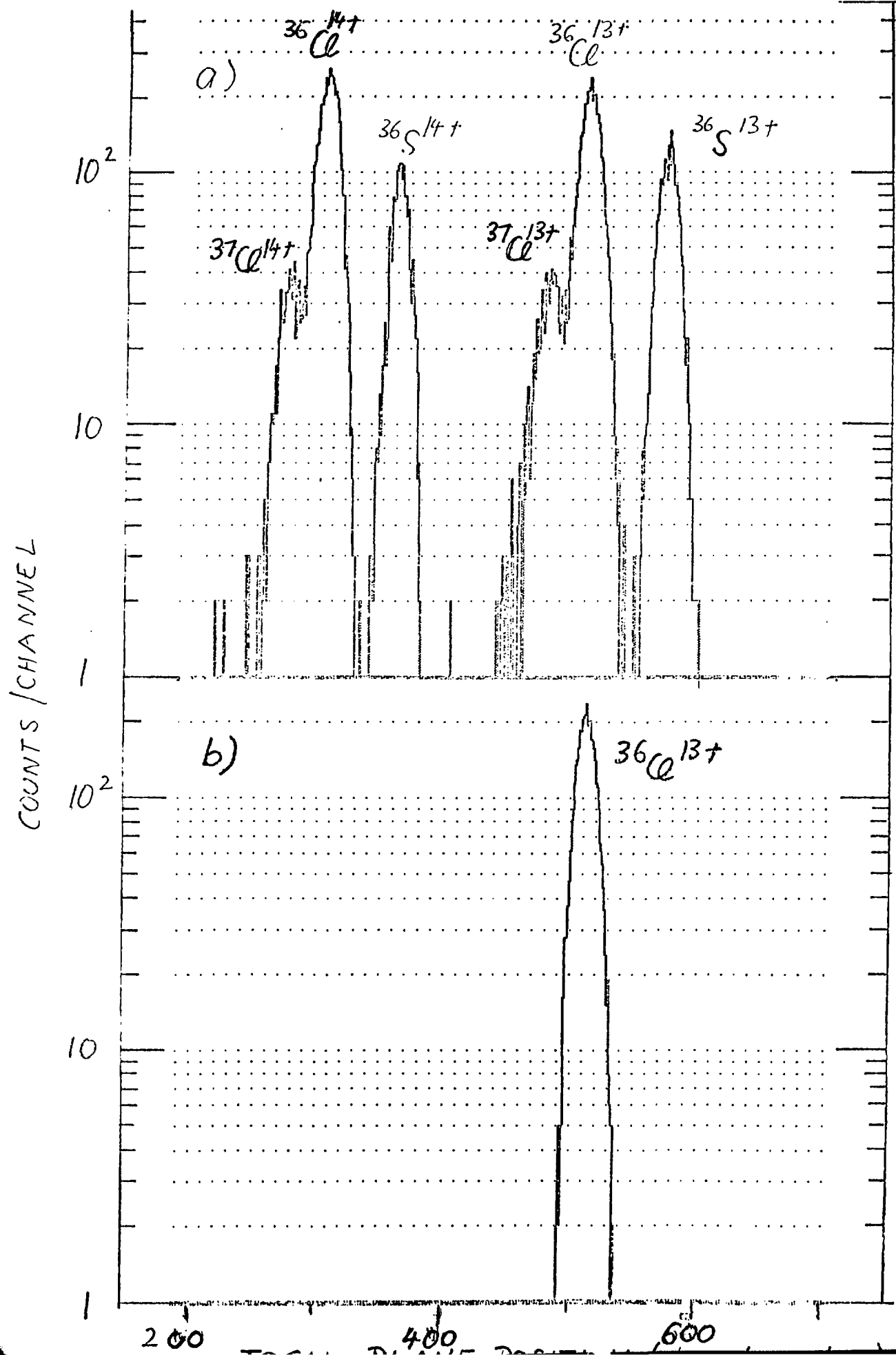
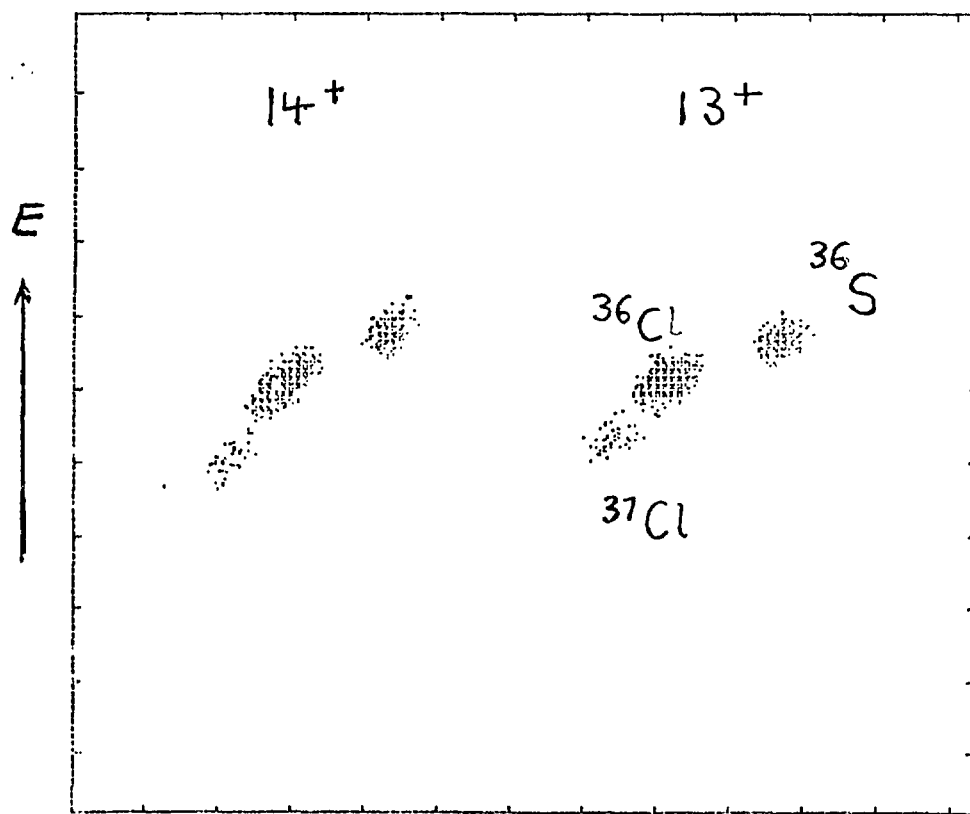
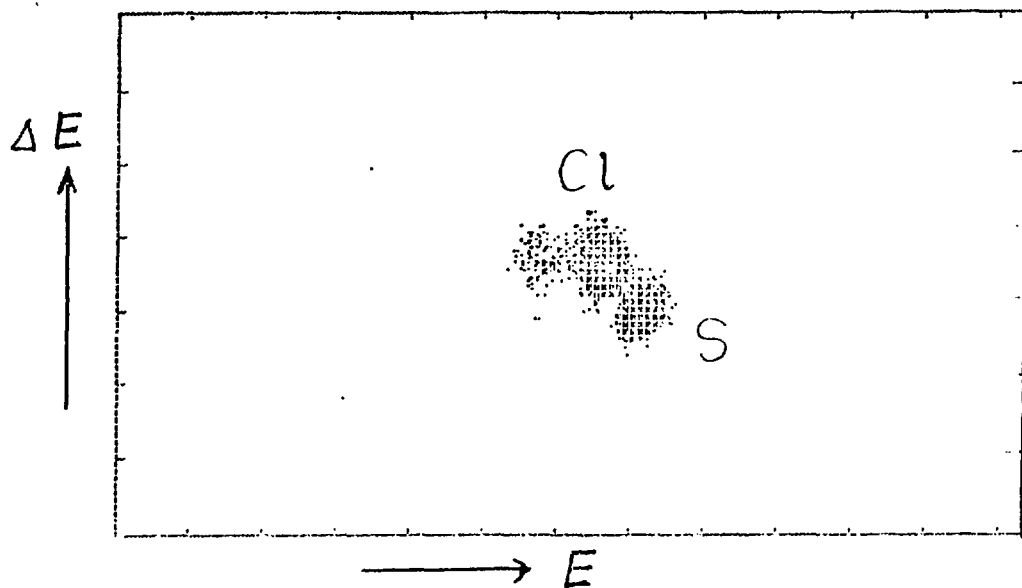


Fig. 17





→ FOCAL PLANE POSITION (B_p)

